*Revised Manuscript (including Abstract)
Click here to view linked References

Modelling and simulation of self-ordering in anodic porous alumina

Chuan Cheng[*], A.H.W. Ngan

Department of Mechanical Engineering, The University of Hong Kong, Pokfulam Road, Hong Kong, P. R. China.

ABSTRACT

Real-time evolution of pre-textured anodic porous alumina growth during anodization is numerically simulated in two-dimensional cases based on a kinetic model involving the Laplacian electric field potential distribution and a continuity equation for current density within the oxide body. Ion current densities governed by the Cabrera-Mott equation in high electric field theory are formed by ion migration within the oxide as well as across the metal/oxide (m/o) and oxide/electrolyte (o/e) interfaces, and the movements of the m/o and o/e interfaces due to oxidation and electric field assisted oxide decomposition, respectively, are governed by Faraday's law. Typical experimental results, such as linear voltage dependence of the barrier layer thickness and pore diameter, time evolution of the current density, scalloped shape of the barrier layer, and the extreme difference in the reaction rates between pore bottoms and pore walls, are successfully predicted. Our simulations revealed the existence of a domain of model parameters within which pre-textured porous structures which do not satisfy self-ordering configurations are driven into self-ordering configurations through a

---

[*] Corresponding author. Tel.: +852 2859 7900; fax: +852 2858 5415
E-mail address: chuan@hku.hk (Chuan Cheng)

self-adjustment process. Our experimental results also verify the existence of the self-adjustment process during anodization.

Keywords: anodic porous alumina; numerical simulation; electric field assisted process; self-ordering

The full title of the journal submitted to: **Electrochimica Acta**

1. Introduction

Anodic porous alumina which can be formed by anodization of aluminum in an acidic electrolyte has received increasing attention both experimentally and theoretically [1-5]. Due to the periodic hexagonal arrangement of the nano-pore channels, relatively ease to control the structures by anodization conditions, excellent thermal stability and low cost, anodic porous alumina has been used extensively as a nanostructured material or as templates to fabricate others, such as photonic crystals [6], nano-wire arrays [7], nano-tubes [8] and nano-capacitors [9].

Although the formation mechanism of anodic porous alumina has been extensively investigated for more than six decades, no generally accepted theory has been established. An electric field assisted dissolution mechanism was first proposed by Hoar and Mott [10], and further developed by O'Sullivan and Wood [1], in which pore formation was due to a competition between oxide formation in the barrier layer and electric field assisted dissolution of oxide at the pore base. However, oxygen tracer experiments [10] demonstrated that at the pore base the oxide was removed by electric field assisted oxide decomposition but not a previously surmised field assisted dissolution mechanism [1], because negligible oxygen loss at the oxide/electrolyte (o/e) interface was detected [11,12]. A recrystallization theory associated with the electro-expansion in the oxide bulk, electro-compression in the oxide/electrolyte interface and variable oxide density across the barrier layer has been proposed to explain the nucleation of porous structures [13].

Several models for porous alumina formation in different mathematical forms have been proposed recently. Parkhutik and Shershulsky [14] proposed a model in which space charge within the oxide body was neglected, and the electric potential distribution obeyed the Laplace equation within oxide. In addition, the o/e interface movement was due to the combination of oxide formation and field assisted dissolution [14], which was in contrast with experimental results that new oxide was only formed at the metal/oxide (m/o) interface [12]. Similar models were further developed by Thamida and Chang [15] and Singh *et al.*[16,17]. However, these models [13-16] were challenged recently by Friedman *et al*. [18,19], who found experimentally that the interpore distance was independent of the electrolyte *pH* value at constant anodization voltage [18], whereas these models [14,15] predicted that the interpore distance should vary with the *pH*.

From tungsten tracer experiments [20,21], an oxide plastic flow mechanism was proposed in which the oxide at the pore base flows towards the pore walls under the mechanical energy during anodization. Houser and Hebert [5] further proposed a mathematical model for the steady state growth of anodic porous alumina. Their calculated results are in good agreement with the experimental tungsten tracer distribution [20,21]. However, as discussed by Oh [22] the tracer study alone cannot yield sufficient evidence to prove oxide flow or disprove electric field assisted dissolution as the mechanism for pore formation, and a close examination [22] of the boundary conditions used in Ref. [5] would show that the new oxide would be generated at the o/e interface, which is inconsistent with the experimental observation that the new oxide only forms at the m/o interface [12,22]. Overmeere *et al.* [23] recently performed an energy-based perturbation analysis, and found that the electrostatic energy, rather than the strain energy-induced surface instability, was the main driving force for pore initiation as well as a controlling factor for pore spacing selection.

Up to now, quantitative investigation of the high electric field (~ 1 V nm^{-1}) behavior within anodic porous alumina by direct numerical calculation has been very limited [15-17,24]. As far as we are aware of, there has been no direct numerical simulation reported on the real-time evolution of the porous structure during anodization. To investigate whether the factor of electric field alone can result in the porous structure growth as well as self-arrange toward ordering, in this paper, we propose a new kinetics model with a group of equations. Numerical implementation of this model is performed by a finite element method in order to capture the real-time evolution of the porous structure growth starting from pre-textured two-dimensional (2D) porous configurations. The kinetics model based on previous theories and experiments will be established first in Sec. 2, and then simulation results will be shown and discussed in Sec. 3.

2. Model for anodic porous alumina formation

2.1. Electric potential distribution

In the present model, space charge within the oxide bulk during anodization is neglected following Parkhutik and Shershulsky [14], Thamida and Chang [15], and Singh *et al.* [16,17]. Thus, the electric potential φ within the oxide obeys the Laplace Equation:

$$\nabla^2\varphi = 0\,. \tag{1}$$

In addition, because the electric conductivities of aluminum and the electrolyte are much larger than the oxide, we assume that the main potential drop is consumed within the oxide. In this paper, the anodization process is simulated under a constant voltage condition. The electric potential at the m/o interface is assumed to have the same value as the anodization voltage V_0. According to Houser and Hebert [24], the overpotential at the o/e interface is far smaller than the anodization voltage, so that the potential there is set to be zero. Moreover, along the right and left edges of a simulation sample (e.g. the vertical dash dotted lines in Fig. 1), a Neumann boundary condition is used. Thus, the boundary conditions are summarized as

$$\begin{cases} \varphi = 0, & \text{at m/o interface} \quad (2) \\ \varphi = V_0, & \text{at o/e interface} \quad (3) \\ \mathbf{n}\cdot\nabla\varphi = 0, & \text{at both edges of the sample} \quad (4) \end{cases}$$

where **n** is the outward normal unit vector for each sample edge. The electric field is given as

$$\mathbf{E} = -\nabla\varphi . \tag{5}$$

The continuity requirement of the steady state ion current density **j** within the oxide bulk can be expressed as follows [14-17]

$$\nabla \cdot \mathbf{j} = 0 \tag{6}$$

From the above equations, we can derive the relationship between the electric field and current density along the electric field lines across the oxide barrier layer, which will be used later. Electric field lines are always perpendicular to equipotential contours within the oxide bulk. Consider a very small cylinder with volume V_c ($V_c \to 0$), which starts from the m/o interface to the o/e interface along an electric field line across the oxide barrier layer. The top and bottom surfaces of the cylinder are elements of the o/e and m/o interfaces with areas represented as $S_{o/e}$ and $S_{m/o}$, respectively. $S_{o/e}$ and $S_{m/o}$ are not equal because of the scalloped shape of barrier layer. The side surface S_{side} of the cylinder is along the electric field line, so that its outward normal vector is perpendicular to the electric field line. From Eqs. (1) and (5), $\nabla \cdot \mathbf{E} = 0$, and with Gauss's Theorem $\oiiint_{V_c} (\nabla \cdot \mathbf{E})\, dV = \oiint_{S_c} (\mathbf{E} \cdot \mathbf{n}) dS$, we have

$$\iint_{S_{o/e}} (\mathbf{E} \cdot \mathbf{n}) dS_{o/e} + \iint_{S_{m/o}} (\mathbf{E} \cdot \mathbf{n}) dS_{m/o} + \iint_{S_{side}} (\mathbf{E} \cdot \mathbf{n}) dS_{side} = 0 . \tag{7}$$

Since $\mathbf{E} \cdot \mathbf{n} = 0$ over S_{side}, $\mathbf{E} = \mathbf{n} E_{o/e}$ over $S_{o/e}$, and $\mathbf{E} = -\mathbf{n} E_{m/o}$ over $S_{m/o}$, where $E_{o/e}$ and $E_{m/o}$ are the electric field intensities at $S_{o/e}$ and $S_{m/o}$, respectively, and as $S_{o/e}$ and $S_{m/o}$ both tend to zero, Eq. (7) becomes

$$E_{o/e} S_{o/e} = E_{m/o} S_{m/o} \tag{8}$$

where $S_{o/e}$ and $S_{m/o}$ are connected by the same electric field line. By virtue of Eq. (6) which is of the same form as $\nabla \cdot \mathbf{E} = 0$, the above procedure can be repeated for **j** to give

$$j_{o/e}S_{o/e} = j_{m/o}S_{m/o} \tag{9}$$

where $j_{o/e}$ and $j_{m/o}$ are the current density magnitudes at $S_{o/e}$ and $S_{m/o}$ respectively. From Eqs. (8) and (9), we obtain

$$\frac{j_{o/e}}{j_{m/o}} = \frac{E_{o/e}}{E_{m/o}}. \tag{10}$$

The same derivation process actually holds for any point within the oxide bulk with electric field intensity E_{bulk} and current density j_{bulk},

$$\frac{j_*}{j_{bulk}} = \frac{E_*}{E_{bulk}} \tag{11}$$

where the subscript "$*$" represents either "o/e" or "m/o, and the oxide bulk point and the o/e or m/o interface point should be connected by the same electric field line. Equation (10) was first cited in Ref. [14] without proof, and its significance, together with that of Eq. (11), is as follows. For a given porous alumina structure, the electric field intensities can be solved directly from Eqs. (1-5). After that, regardless of whether the rate determining step of the anodization process is at the o/e interface, oxide bulk, or m/o interface, if we can calculate the current density at one location, e.g. the o/e interface, we can obtain the current density at other two locations by using Eqs. (10) and (11) directly. The location at which the current density is first evaluated may not necessarily be the location at which the rate determining step occurs, but the calculated current density will be controlled by the rate determining step through Eq. (11). Here, we assume that ion migration across the o/e interface is the rate determining step, because the oxygen and aluminum ions are weakly bound under the effect of the high electric field [1]. It should be noted that ionic migration in the bulk oxide has been proposed previously as an alternative rate determining step [13], but recent experiments revealed that an increase in the electrolyte's acid concentration, which should play a role directly at the o/e interface, can influence the anodization process significantly, such as increasing the pore diameter [25], the current density [26], and the oxide growth rate [18]. These profound changes of the anodization process should be due to anodization condition changes at the o/e interface, and this is the basis of the present assumption that the rate determining step is at this interface. In Sec. 2.2, the current density at the o/e interface is derived at first, and then the current density at the m/o interface is obtained from Eq. (10). Based on these, the interface movement equations are established from Faraday's Law. Sec. 2.3 provides parameter values used in the following simulations.

2.2. Ion current density at both interfaces and interface movement equations

In anodic porous alumina formation, oxygen transport study using nuclear microanalyses of O^{18} and O^{16} concluded that new oxide forms only at the m/o interface but not elsewhere [12], which implies that the oxidation reaction within the oxide body is negligible. On this basis we assume that electrochemical reactions take place only at interfaces, and the ions migrating from one interface to another are not consumed on their way. On both o/e and m/o interfaces, as shown in Fig. 1, the most possible reactions based on previous experiments are provided, and behind each reaction is the corresponding ion current density. As the electrochemical reaction rates are much faster than the ion migration rates [27,28], the ion current density during anodization is restricted by ion migration. In the following, aluminum and oxygen ion migration will be considered separately.

First, for the aluminum ions they migrate into the electrolyte at the o/e interface, and they come from two sources. The first source is the net loss of aluminum ions from the m/o interface (by reaction R1 in Fig. 1), migrating across the oxide barrier layer, and then ejecting into the electrolyte (by reaction R2 in Fig. 1) without oxide formation at the o/e interface [12,29]. The current density due to this source is denoted as $\mathbf{j}_{Al,ox}$, where "ox" means the corresponding ions migrating through the oxide body, and the values of $\mathbf{j}_{Al,ox}$ at the o/e and m/o interfaces are denoted as $\mathbf{j}_{Al,ox}|_{o/e}$ and $\mathbf{j}_{Al,ox}|_{m/o}$, respectively. The second source of aluminum loss comes from electric field assisted oxide decomposition at the o/e interface (by reaction R3 in Fig. 1) [11], and then ejection into electrolyte by reaction R2 in Fig. 1, to form current density $\mathbf{j}_{Al,dis}$. At the same time, the formed oxygen ions by R3 (with current density $\mathbf{j}_{O,dis}$) will migrate towards the m/o interface to form new oxide, but not lose into electrolyte because negligible oxygen loss from oxide to electrolyte was found by experiments [11]. $\mathbf{j}_{Al,dis}$ and $\mathbf{j}_{O,dis}$ are equal, but the corresponding ion movements are in opposite directions, i.e.

$$\mathbf{j}_{Al,dis} = \mathbf{j}_{O,dis}. \tag{12}$$

Considering the above two sources of aluminum ions, at the o/e interface, the total aluminum ion current density is written as

$$\mathbf{j}_{Al,o/e} = \mathbf{j}_{Al,ox}\Big|_{o/e} + \mathbf{j}_{Al,dis}. \tag{13}$$

At the o/e interface, although the aluminum ions ejected into the electrolyte come from two sources, their migration under the electric field across the o/e interface is the same since they are the same species. Physically, this process is governed by the Cabrera-Mott equation in the high electric field theory [27,28,30],

$$\mathbf{j}_{Al,o/e} = n_{Al} A_{Al} \exp(k_{Al} E_{o/e}) \hat{\mathbf{E}}_{o/e} \tag{14}$$

where $A_{Al} = C_{H^+}^{\eta} q_{Al} \nu_{Al} \exp\left(-W_{Al}/kT\right)$ and $k_{Al} = \alpha_{Al} q_{Al} a_{Al}/kT$. Here, n_{Al} is the density of mobile aluminum ions at the o/e interface, q_{Al} is the charge of one aluminum ion, v_{Al} is the vibration frequency of aluminum ions, W_{Al} is the potential barrier without electric field at the o/e interface, α_{Al} is a transfer coefficient related to the symmetry of the potential barrier, a_{Al} is the jump distance (twice the activation distance) of aluminum ions, k is the Boltzmann constant, T is the absolute temperature, and $\hat{\mathbf{E}}_{o/e} = \mathbf{E}_{o/e}/E_{o/e}$ is the unit vector of electric field $\mathbf{E}_{o/e}$ at the o/e interface. Here, following Refs. [14-17] to describe the fact that the electric field assisted process is strongly influenced by the acid concentration at o/e interface, the current density is scaled by a factor $(C_{H^+})^{\eta}$, where C_{H^+} is the proton concentration, and η = 1 according to Refs. [14-17]. Some uncertainties about the term $(C_{H^+})^{\eta}$ may exist, but these do not influence the substance of the model, because the term $(C_{H^+})^{\eta}$ is absorbed into the parameter A_{Al} in Eq. (14), which is then absorbed into another parameter $B_{Al} = n_{Al}^{0} A_{Al}$ in Sec. 2.3, i.e. B_{Al} is the eventual model parameter used. In Sec. 3.2 below, we predict the regime of the B_{Al} parameter within which stable pore growth can occur, and by regarding a change in B_{Al} as arising from a change in the acid concentration in accordance with Eq. (14), good qualitative agreement with experimental observations can be made. This proves that although the actual dependence of A_{Al} on the acidity may not be represented exactly by the $(C_{H^+})^{\eta}$ term, A_{Al} should at least be an increasing function of C_{H^+}.

Secondly, for oxygen ions, they are responsible for new oxide formation at the m/o interface by reaction R4 in Fig. 1, and they migrate to this interface from the o/e interface. Their current density across the oxide body is denoted as $\mathbf{j}_{O,ox}$, and the local value of $\mathbf{j}_{O,ox}$ at the o/e and m/o interfaces are denoted as $\mathbf{j}_{O,ox}|_{o/e}$ and $\mathbf{j}_{O,ox}|_{m/o}$, respectively. At the o/e interface, $\mathbf{j}_{O,ox}|_{o/e}$ is also contributed from two sources. One is from water decomposition at the o/e interface (by reaction R5 in Fig. 1) [11,12], the current density of which is denoted as $\mathbf{j}_{O,o/e}$. The other source is from decomposition of old oxide at the o/e interface by reaction R3 in Fig. 1, and as mentioned before, the current density of which is $\mathbf{j}_{O,dis}$ (= $\mathbf{j}_{Al,dis}$). Thus,

$$\mathbf{j}_{O,ox}\Big|_{o/e} = \mathbf{j}_{O,o/e} + \mathbf{j}_{O,dis}. \tag{15}$$

After oxide decomposition by reaction R3 in Fig. 1, the oxygen ions will not lose into the electrolyte but will migrate towards the m/o interface to form new oxide [11]. Thus, only those oxygen ions coming from water decomposition (with current density $\mathbf{j}_{O,o/e}$) need to jump across the potential barrier at the o/e interface, and this current density should also follow the Cabrera-Mott equation [27,28,30], which is

$$\mathbf{j}_{O,o/e} = n_O A_O \exp(k_O E_{o/e})\hat{\mathbf{E}}_{o/e} \tag{16}$$

where $A_O = q_O \nu_O \exp\left(-W_O / kT\right)$ and $k_O = \alpha_O q_O a_O / kT$, and the parameters in these expressions have similar meanings as in Eq. (14) albeit now for O^{2-} ions. From Eqs. (14) and (16), the total ion current density across the o/e interface is

$$\mathbf{j}_{total,o/e} = \mathbf{j}_{Al,o/e} + \mathbf{j}_{O,o/e} = \left[n_{Al} A_{Al} \exp\left(k_{Al} E_{o/e}\right) + n_O A_O \exp\left(k_O E_{o/e}\right)\right]\hat{\mathbf{E}}_{o/e} . \tag{17}$$

Thirdly, according to the above discussion, continuous growth of porous alumina depends on the outward migration of aluminum ions and inward migration of oxygen ions across the oxide barrier layer. In experiments, under a certain anodization condition, the transport numbers of both aluminum and oxygen ions were found to be fixed [11,31], so that the ion current densities due to the transport of aluminum and oxygen ions should also be fixed, i.e.

$$\beta = \frac{\left. j_{Al,ox}\right|_{m/o}}{\left. j_{O,ox}\right|_{m/o}} = \frac{\left. j_{Al,ox}\right|_{o/e}}{\left. j_{O,ox}\right|_{o/e}} , \tag{18}$$

where β is a constant value, and each j is the current density magnitude corresponding to that current density $\mathbf{j}$. “ox” also means the corresponding ions migrating through the oxide body. In achieving the second step in Eq. (18), Eq. (10) is used. As a typical condition, we set β to be 3/7 for our simulation, in accordance with experimental results [11]. From Eqs. (12), (13), (15) and (18), and noting that $\mathbf{j}_{Al,ox}|_{o/e}$, $\mathbf{j}_{O,ox}|_{o/e}$, $\mathbf{j}_{Al,o/e}$, $\mathbf{j}_{O,o/e}$, $\mathbf{j}_{Al,dis}$, and $\mathbf{j}_{O,dis}$ have the same direction $\hat{\mathbf{E}}_{o/e}$ at a given point on o/e interface,

$$\mathbf{j}_{Al,dis} = \frac{j_{Al,o/e} - \beta\, j_{O,o/e}}{1+\beta}\hat{\mathbf{E}}_{o/e} . \tag{19}$$

Finally, from Faraday’s law [27,28], the change in volume V of the oxide caused by a passed charge Q carried by ions is

$$V = \frac{MQ}{zF\rho} = \frac{MAjt}{zF\rho} \tag{20}$$

where M is the molecular weight of oxide Al_xO_y, $z = xy$, ρ is the oxide density, j is the partial current density corresponding to the reaction, A is the area of oxide surface, t is time and F is Faraday’s constant. Thus, the moving velocity $\mathbf{v}$ of the oxide thickness

$D = V/A$ at a given point at the interface is proportional to the current density as

$$\mathbf{v} = -\frac{dD}{dt}\hat{\mathbf{E}} = -\frac{M}{zF\rho} j\hat{\mathbf{E}}. \tag{21}$$

where $\hat{\mathbf{E}} = \mathbf{E}/E$ is the unit vector of the electric field. Equation (21) is not only suitable for the m/o interface where the oxidation reaction (R4 in Fig. 1) takes place but also for the o/e interface movement where the oxide decomposition reaction (R3 in Fig. 1) takes place. The moving velocity direction is in the opposite direction of the electric field at a given point on the interface. More specifically, at the o/e interface, the interface movement velocity is $\mathbf{v}_{o/e} = -\, \mathbf{j}_{Al,dis}M/zF\rho$, and substituting in Eq. (19), and replacing $\mathbf{j}_{Al,o/e}$ and $\mathbf{j}_{O,o/e}$ by Eqs. (14) and (16), respectively, we obtain

$$\mathbf{v}_{o/e} = -\frac{M}{zF\rho(1+\beta)}[n_{Al} A_{Al} \exp(k_{Al} E_{o/e}) - \beta n_o A_o \exp(k_o E_{o/e})]\hat{\mathbf{E}}_{o/e}. \tag{22}$$

Similarly, the m/o interface movement velocity is $\mathbf{v}_{m/o} = -\, \mathbf{j}_{O,ox}|_{m/o}M/zF\rho$, and from Eqs. (10), (12), (14), (15), (16), and (19), this is given as

$$\mathbf{v}_{m/o} = -\frac{M}{zF\rho(1+\beta)}\frac{E_{m/o}}{E_{o/e}}[n_{Al} A_{Al} \exp\left(k_{Al} E_{o/e}\right) + n_O A_O \exp\left(k_O E_{o/e}\right)]\hat{\mathbf{E}}_{m/o}. \tag{23}$$

2.3. Simulation parameters

n_{Al} and n_O are mobile ion densities at the o/e interface, which are used in Eqs. (22) and (23). It was experimentally established that the change of mobile ion density depends exponentially on the electric field intensity (see Fig. 14 in Ref. [28]). A cutoff electric field intensity (E_{cutoff} = 1.1 V nm^{-1}) was predicted, above which all ions become mobile [28]. According to the Cabrera-Mott equation [27,28,30], the condition of “all ions being mobile” means that all ions have the possibility to jump over the potential barrier under E_{cutoff}, but at one time only a fraction of them realize the migration. Following these observations, in our simulations the following equation was used to represent the electric field dependent mobile ion density for both ion species (for oxygen ions the subscript Al is replaced with O):

$$n_{Al} = n_{Al}^{0} \exp\left[\ln(\lambda) - \ln(\lambda)\frac{E_{o/e}}{E_{cutoff}}\right], \tag{24}$$

where n_{Al}^{0} is the number of aluminum ions when all of them are mobile, and $\lambda = 0.2$. Other λ values (e.g. 0.1 and 0.5), were also used in the simulation, but no significant change in the results was found compared with 0.2, because at the pore base the electric field intensity is always around 1 V nm^{-1}. Although Eq. (24) is empirical in nature, but the described trend of the ion density as shown in Fig. 2 is nevertheless in good accordance with experiments [28]. The dependence of the mobile ion density on the electric field certainly deserves further theoretical investigation, and when a more realistic model is established in the future, this can replace Eq. (24).

In addition, as observed in experiments [32], at the o/e interface, a double logarithmic plot of the oxygen ion current density $j_{O,o/e}$ versus the aluminum ion current density $j_{Al,o/e}$ yielded straight lines corresponding to $\left(\partial \ln j_{O,o/e} / \partial \ln j_{Al,o/e}\right)_{pH} = 1.38(\pm 0.14)$, where the slope 1.38 is rather independent of the pH value from 0 to 11. Thus, from this relation and Eqs. (14) and (16) we set $k_O/k_{Al} = 1.5$ in our simulations. k_O was set to be 3.8 nm V^{-1}, which has the same order of magnitude as used in Ref. [14]. For the oxide density ρ used in Eqs. (22) and (23), although recent investigations [13,33] showed that ρ was different at the o/e and m/o interfaces, it is not clear whether and how the oxide density varies along each interface, and for simplicity's sake a constant oxide density 3.118 g cm^{-3} is used, which is in the range of experimental values [28,31]. Position dependent oxide density along each interface can be adopted easily in the present model when the exact relation is clear in the future.

Furthermore, the exact values of n_{Al}^{0}, n_{O}^{0}, A_{Al} and A_{O} for porous-type anodic alumina are hard to measure in experiments. Although these values have been evaluated for barrier-type anodic alumina [28], they cannot be used directly for porous-type anodic alumina as their formation conditions are very different. In order to reduce the complexity, we set

$$B_{Al} = n_{Al}^{0} A_{Al} = n_{Al}^{0} C_{H^+}^{\eta} q_{Al} \nu_{Al} \exp\left(-W_{Al} / kT\right) \qquad (25)$$

$$B_{O} = n_{O}^{0} A_{O} = n_{O}^{0} q_{O} \nu_{O} \exp\left(-W_{O} / kT\right) \qquad (26)$$

as constants under a certain anodization condition, where the various parameters have been explained previously in Eqs. (14), (16), and (24). The values of B_{Al} and B_{O} were estimated based on reported values [28] for each of the parameters involved in B_{Al} and B_{O} to produce growth rates on the order of 1 nm s^{-1} at the pore base, which is a common experimental value under mild anodization conditions [2,4]. For example, to investigate the stability range of the pore growth (see Fig. 7(a) later), B_{Al} and B_{O} were varied within the ranges [0.12, 1.5] A m^{-2} and [0.024, 0.12] A m^{-2}, respectively. Here, the typical condition of B_{Al} = 1 A m^{-2}, for instance, can be achieved by setting the charge density $n_{Al}^{0} q_{Al}$ = 1800 C cm^{-3}, vibration frequency ν = 10^{12} s^{-1}, temperature T = 275 K, pH = 1, η =1 and potential barrier W_{Al} = 1.105 eV. These quantities are physically reasonable according to Ref. [28]. Similarly, the B_{O} value in the range

[0.024, 0.12] A m^{-2} can also be rationalized by reasonable values for the parameters involved in Eq. (26).

3. Simulation results and discussion

Numerical calculation was done to simulate the real-time evolution of 2D porous alumina growth starting from pre-textured porous configurations. Simulations are realized based on a finite element method to solve the model equations in Sec. 2, by using a computer code developed from the Matlab PDE toolbox [34]. As both the o/e and m/o interfaces grow with increasing anodization time, the calculation region (the oxide body) gets modified, and so remeshing was performed after the interface movement at each time step Δt. Different time intervals $\Delta t \in [0.01, 1]$s were attempted, and negligible differences were found among the results when $\Delta t \leq 0.1$ s. Thus, Δt = 0.1 s was used in all of the simulations reported here.

Section 3.1 below focuses on electric field driven pore growth, in which typical length scales of the porous structures, oxide growth rates, and current densities are obtained. Section 3.2 focuses on electric field driven self-ordered porous structure growth. Comparison between our simulation and previous experiments are provided in both sections, and especially in Sec. 3.2 we also provide our own experimental results for comparison.

3.1. Electric field driven porous structure growth

It has been well established from experiments that under conditions of, say, 0.3 M oxalic acid and 40 V anodizing voltage, steady state self-ordering pore growth happens with both barrier layer thickness and pore size of about 40 nm, and interpore distance of about 100 nm [2,4,35]. In order to compare with these conditions, we performed the simulation as shown in Fig. 3. The initial configuration (at t = 0) is shown in Fig. 3(a): the sample width, height, and barrier layer thickness were 200, 50, and 40 nm, respectively; two initial pores with diameter and interpore distance 20 and 100 nm were placed at the o/e interface; and the m/o interface was initially flat without scalloped shape.

As shown in Figs. 3(a-d), the electric field distribution was calculated from Eqs. (1-5) and plotted within each porous structure. From Fig. 3 (b), along the o/e interface the fastest oxide growth rate happens at the pore bottom, while the top surface as well as the pore walls, which are far from the pore bottom, have very small growth rates. This is because the pore bottom has higher electric field intensity than other parts of the o/e interface, and the interface movement velocity is exponentially dependent on electric field intensity (Eq. (22)). Along the m/o interface, faster growth rate also happens at the pore bottom, because the current densities at the o/e interface, the oxide bulk, and the m/o interface must coordinate with each other according to Eqs. (10) and (11). As time increases, the typical scalloped shape of the oxide barrier layer observed in experiments [4,35], as well as the water drip pore shape observed at the beginning stage of anodization process [1], were reproduced in the present simulation (see Fig. 3(c)). From Fig. 3(d), it is obvious that most of the applied electric field potential is consumed within oxide barrier layer, while only a small part of it is consumed within the pore walls. This kind of potential distribution is an inevitable outcome when solving the Laplace equation over a domain with finger-like features. As the growth rate is exponentially depending to electric field (Eqs. (22) and (23)), the extremely large difference in the growth rates between the barrier layer and the pore base as observed in experiments [36] is a consequence of the large difference in driving force due to the electric field distribution within the oxide body according to our simulation. From Fig. 3(d), the steady state barrier layer thickness, pore diameter, and pore growth rate are about 41.2 nm, 35.9 nm, and 0.94 nm s^{-1}, respectively, and these correspond very well to experiments [2,4,35]. In addition, simulations with an initial barrier layer thickness of 20 nm, as opposed to the 40 nm in Fig. 3(a), have also been done. Similar length scales of the porous structure are obtained under the same simulation parameters as in Fig. 3, e.g. the obtained steady state barrier layer thickness is about 41.7 nm which is very close with the 41.2 nm obtained in Fig. 3 for an initial barrier thickness of 40 nm.

In experiments, an apparent current density is usually reported as the total anodizing current divided by the initially flat (i.e. apparent) sample area, instead of the actual surface area corresponding to the scalloped geometry of the barrier layer [36], and so to enable direct comparison the same measure was adopted in our simulation. First, the total ion current was calculated by integrating along the o/e interface the actual current density $\mathbf{j}_{total,o/e}$ evaluated from Eq. (17), and this is then divided by the sample width to obtain the apparent current density. In Fig. 3(e), the current density evaluated at each time step in the simulation shown in Figs. 3(a-d) is plotted against the simulation time. It can be seen that the current density exhibits some fluctuations with increasing time, and these are due to the discretization of the o/e interface – with time increasing, the o/e interface is lengthening due to pore growth, and so additional points were added onto the o/e interface, and this procedure results in small changing roughness of the o/e interface with time, which then causes the fluctuations of the calculated current density against time. Even though such an artificial effect exists, a general tendency of the current density versus time is clear – the current density first decreases with time for $t \in [0, 30]$ s, and then it increases quickly between $t \in [30, 75]$ s and finally a steady state value of ~ 21.4 A m^{-2} is achieved for $t > 75$ s. The steady state current density is due to the fact that, in a stable pore growth state such as that shown in Fig. 3(d), the vertical pore walls elongate as time proceeds but the ion current through them is negligible, and the total current is mainly through the pore base which almost does not change shape and area under steady state. Such a trend of the current density versus time is commonly observed in experiments under constant voltage conditions, e.g. in Figs. 8 and 9 of Ref. [37], not only such a trend was observed, but the steady state current density value was also around 20 A m^{-2} under the same anodization voltage 40 V as in our simulation.

In order to investigate the influence of the anodization voltage on the evolution of the porous structure, we performed the simulations shown in Fig. 4. The initial sample configurations were the same as Fig. 3(a), except that the interpore distance was set to scale with the anodization voltage V_0 (in V) as $2.5 \times V_0$ nm, in order to conform to the experimentally observed ratio of interpore distance to voltage of about 2.5 nm V^{-1}

when self-ordered porous patterns were obtained under mild anodization conditions [2,4]. The parameters used in simulation, such as $B_{Al} = 0.72$ A m^{-2} and $B_O = 0.072$ A m^{-2}, are also the same as those in Fig. 3. By comparing the two current density curves in Fig. 4(a), we can see that a higher anodization voltage results in (i) a shorter time to reach steady state, (ii) a higher steady state current density, and (iii) a sharper rise of the current density at the critical time period between minimum current density and the first establishment of the steady state. All these three phenomena are in good agreement with experimental observations, such as Fig. 16 in Ref. [38]. In Fig. 4(b), the steady state current density, calculated as the average value of the current density in the steady state regime, increases with the anodization voltage, and so does the growth rate at the pore base. In experiments, it has been reported that the steady state current density increases exponentially with the anodization voltage [26]. Our simulated steady state current density does not increase as quickly as exponentially with voltage, probably because the simulated voltage range is too narrow, or because some of the simulation parameters, on which the current densities depend exponentially, are set smaller than the real values, but the increasing trend is correct.

Figure 5 shows the dependence of steady state barrier layer thickness and the pore diameter on the anodization voltage. As can be seen the simulated trends are linear, and the barrier layer thickness to voltage ratio, as well as the pore diameter to voltage ratio, are both around 1 nm V^{-1}. Such linear relationships are typical results found in anodization experiments [1,4], our numerical simulations reproduce them well.

3.2. Electric field driven self-ordered growth of porous structures

In our simulations, only under certain choice of the simulation parameters the initial pre-textured self-ordering pattern can be maintained and developed into high aspect ratio pore channels as time proceeds. Also, in previous anodization experimenters [40], which started from pre-textured aluminum surfaces, long straight pores with high aspect ratios can only be obtained within a narrow window of processing conditions. We therefore believe that these parameters in our simulations should correspond to such a window of processing conditions for high self-ordering, and in this section, we aim to establish a map of these parameters for different growth regimes. After that, parameters within the stable porous regime will be chosen for simulations with incompatible or disordered pre-texturing of the initial pore nuclei, to study the ability of the electric field in driving these structures into a self-ordered growth mode.

As an example, Figs. 6(a-d) show four simulated porous structures after 300 s of anodization, starting from the pre-textured configuration shown in Fig. 3(a). The B_{Al} value is equal to 0.12, 0.36, 0.54, and 0.78 A m^{-2} for Figs. 6(a-d), respectively; while other parameters such as the anodization voltage 40 V and B_O = 0.048 A m^{-2} are the same for these four simulated cases. Fig. 6(e) shows the current density versus time relations corresponding to Figs. 6(a-d), respectively. In Fig. 6(a), the two initial pores almost do not grow within 300 s, and the barrier layer also stops to grow after reaching a 64 nm thickness. Thus, the oxide layer can be regarded as barrier-type alumina in which no porous structure is formed during anodization. The corresponding current density in Fig. 6(e) decreases towards zero with increasing time. On the other hand, after increasing B_{Al} to 0.36 A m^{-2} and 0.54 A m^{-2} (Fig. 6(b) and 6(c)), the two initial small pores develop into ordered deep pores with barrier layer thickness 48.3 nm and 38.9 nm, and pore diameter 32.4 nm and 38.6 nm, respectively. Their corresponding current densities in Fig. 6(e) first decrease and then increase to a steady state value. By increasing B_{Al} to 0.78 A m^{-2} (Fig. 6(d)), although the initial pores grow into deep ones, the initial pore ordering cannot be maintained, with one pore terminating in the middle of the oxide layer while the other splitting into three or more branches. For this case, even if the anodization time is allowed to increase beyond 300 s, the structure is still unstable. The corresponding current density in Fig. 6(e) also decreases at first and then increases later, but then it fluctuates severely with time. From the simulations in Fig. 6, one can see that with B_{Al} increasing anodic alumina can transit from the barrier-type to the porous-type structure, but the porous-type structure can become unstable if B_{Al} is too large. Thus, by changing only the model parameter B_{Al}, the anodic alumina structure can be made to transit between the three regimes of nonporous growth, stable porous growth, and unstable porous growth.

In order to establish a map for the conditions for nonporous, stable porous, and unstable porous growth to happen, simulations were done by changing the parameters B_{Al} and B_O systematically in a wide range, while other model parameters as well as the initial configuration are the same as in Fig. 6. In each simulation, 300 s anodization time were simulated. Whenever the simulation parameters yielded a stable porous structure, the barrier layer thickness, pore diameter, steady state current density and pore-bottom growth rate were plotted in Fig. 7.

From Fig. 7(a), under a constant B_O, for example 0.096 A m^{-2} (hollow triangle symbols), stable porous growth happen when B_{Al} is from 0.3 to 1.2 A m^{-2}, and lower values of B_{Al} lead to nonporous alumina, while higher B_{Al} values lead to unstable porous alumina. With B_O increasing, the range of B_{Al} corresponding to stable porous growth also increases. In addition, in Fig. 7(a), the nonporous-stable porous regime boundary (dash dotted line), and the stable-unstable porous regime boundary (dash line) are both linear. Fig. 7(b) shows the relationship between the barrier layer thickness and B_{Al}, while B_O is kept constant for each curve in the figure. It is clear that under each constant B_O, the barrier layer thickness decreases with B_{Al} increasing. Under any constant B_O value (independent with B_O), there exists a cutoff barrier layer thickness value of 36.6 nm, below which the porous structure cannot maintain stable development during anodization. As a constant anodization voltage of 40 V was used in simulation, the corresponding cutoff barrier layer thickness to voltage ratio, referred to as the cutoff ratio hereafter, is 0.915 nm V^{-1}. This is an important ratio because below this value a stable porous structure will transit into an unstable porous structure. As only the electric field is considered in our model, the cutoff ratio must take effect by means of electric field intensity within the barrier layer in which the average cutoff electric field intensity is about 1.09 V nm^{-1}. The inset figure in Fig. 7(b) is the relationship between the barrier layer thickness and the B_{Al}/B_O ratio. The data in the five curves in the main panel of Fig. 7(b) can be seen to collapse onto the same curve in the inset figure, except for several points for which the barrier layer is too thick. From the inset figure, we can see that it is the B_{Al}/B_O ratio but not B_{Al} or B_O alone which determines the barrier layer thickness. Figure 7(c) shows the relationship between the pore diameter and B_{Al} under different B_O values. As is similar to the barrier layer thickness, a cutoff pore diameter of about 40 nm seems to exist, above which stable porous structures will transit into unstable porous structures. In Fig. 7(d), the steady state current density, as well as the pore-bottom growth rate shown in the inset figure, both increase with B_{Al} under a constant B_O in a similar fashion. The boundary between the stable and unstable growth regimes becomes a sloping line above which a pre-textured self-ordering pattern cannot grow in a stable fashion. This means that the current density, or the pore-bottom growth rate, cannot be too high for stable porous growth to occur, which is similar with experiments.[1]

In our model, $B_{Al} = n_{Al}^0 A_{Al} = n_{Al}^0 C_{H^+}^{\eta} q_{Al} \nu_{Al} \exp\left(-W_{Al}/kT\right)$ (c.f. Eq. (14)), and so its change can result from parameters such as $C_{H^+}^{\eta}$, v_{Al} and W_{Al}. In order to check whether the term $C_{H^+}^{\eta}(=10^{-pH\eta})$ in Eq. (14) is reasonable, we regard an increase of B_{Al} under a constant B_O as due to an increase of the acid concentration (or decrease of pH). From Figs. 7(b-d), a higher acid concentration can result in thinner barrier layer thickness, larger pore diameter and higher steady state current density. These three trends agree well with experiments– see Fig. 8 (b) of Ref. [1], Fig. 2(a) of Ref. [25], and Fig. 5 of Ref. [41], respectively.

In order to study the self-ordering process of porous structure growth which starts from pre-textures which do not satisfy the 2.5 nm V^{-1} self-ordering condition found in experiments [2,4], the simulations shown in Figs. 8 and 9 were performed. Our experimental comparison is shown in Fig. 10. Simulation parameters are chosen within the stable porous region in Fig. 7. These simulations will reveal the ability of electric field to drive an initial non-self-ordering growth mode into a self-ordering growth mode with increasing anodzation time.

In Figs. 8(a-c), the same simulation parameters as in Fig. 3 were used for all of the three simulated samples. The current density versus time relationships corresponding to the three sample growth cases are shown in Figs. 8(d-f), respectively. In Figs. 8(a) and (c) the initial interpore distance to voltage ratio does not satisfy the 2.5 nm V^{-1} self-ordering condition found experimentally, while that in Fig. 8(b) does. In Fig. 8(b), the two pores grow steadily without changing the initial interpore distance. In Fig. 8(a), the central pore branches to form two pore channels, while in Fig. 8(c), the left and right initial pores stop growing but the central pore undergoes a complicated evolution process to give rise to two eventual pore channels. For all of the three samples, when steady state is reached, the porous scales at the pore bottom region are very similar, which all satisfy the 2.5 nm V^{-1} self-ordering condition, although the initial pre-textures in Figs. 8(a) and (c) do not satisfy such a condition. The cases in Figs. 8(a) and (c) therefore represent a self-arrangement process, in which pre-textures with an interpore spacing incompatible with the anodizing voltage will self-organize into structures with the compatible interpore spacing. In addition, from Figs. 8(d-f), for the pre-texture with the 2.5 nm V^{-1} condition met (2 initial pores), the current density takes the shortest time (75 s) to reach steady state, while other two cases incompatible with such a condition (1 and 3 initial pores) need more time (150 s and 500 s respectively) to reach the steady state. This tendency also agrees with experiments – see Fig. 5 of Ref. [38], or Fig. 2 in Ref. [42], in which the current density in a second-time anodization step (with the compatible pre-texture established in the first anodization step) needed less time to reach steady state than the first-time anodization step.

Numerical simulation of porous structure growth starting from a disordered pre-textured pattern is shown in Fig. 9, which also shows the self-arrangement process driven by electric field. In the pre-texture shown in Fig. 9(a), nine small pores with non-uniform interpore distance as well as diameter are introduced. With time increasing in Figs. 9(b-d), the axes of some pores, which represent the trajectories of the pore bottom parts, do not evolve along straight vertical lines but bend slightly. From the movement of pore bottoms, the electric field tends to drive the configuration towards one in which large interpore distances are reduced and small interpore distances are increased, i.e. an ordered state. At the same time, the pore size also gets more uniform, e.g. the 1st, 4th and 7th pore from the left in Fig. 9(a) are large initial pores, but after growing for 200 s as shown in Fig. 9(d), these pores become smaller at their base. It can be seen that in Fig. 9(d), all the pores have rather similar sizes at their base. In order to observe above ordering tendency more clearly, as shown in Fig. 9(e), the standard deviation of the interpore distance was computed as $SD = \sqrt{(N-1)^{-1}\sum_{i=1}^{N}\left(D_i - \overline{D}\right)^2}$, where D_i is the interpore distance, N is the number of pore pairs, and $\overline{D}$ is the mean of D_i. The pore center position is calculated as the geometrical center of the curved part (or half-circle part) of the o/e interface around the pore base. Fig. 9(e) shows that the standard deviation of the interpore distances decreases from about 7 nm to 2.5 nm in 200 s' anodization time. In experiments [43], under the condition of 0.3 M oxalic acid and 40 V, the standard deviation of interpore distance was about 2.0 to 3.0 nm for anodized 99.5% pure aluminum, and 1.0 to 1.6 nm for anodized 99.9995% pure aluminum, and these values are in accordance with our simulation results at 200 s anodization time.

Experimental verification of the self-arrangement process indicated in Figs. 8 and 9 has also been performed in this work, and the results are shown in Fig. 10. Detailed descriptions of the experimental method can be found in Ref. [44]. In this experiment, only one step of anodization was performed, in which 99.9% pure aluminum foil was anodized in 0.4 M oxalic acid at 2 ^{o}C at 40 V for 20 h. Then, part of the sample was put into a mixed solution of H_2CrO_4, H_3PO_4 and H_2O with composition 1.8 : 6 : 92.2 by weight, at 60^{o}C for about 1 h to remove the porous alumina formed on the aluminum substrate. A Hitachi S-4800 field emission scanning electron microscope was used to obtain Figs. 10(a-c).

Figure 10(a) shows the top view of the anodic porous alumina, which reflects the porous pattern at the beginning stage of anodization. Figure 10(b) shows the side view of the pore channels near the pore bottom region, indicating that the pore channels are very straight and correspond to stable porous structure growth towards the end of the 20h anodization. The scalloped shape of the oxide barrier layer is clearly observed at the pore bottom in Fig. 10(b), and because of this shape each pore will leave behind a small pit on the aluminum substrate. After selectively dissolving the alumina on top, a pitted pattern is left on the aluminum substrate, and this was imaged as shown in Fig.10 (c), which directly reveals the ordering of the pores at the very end of the 20 h anodization. In order to quantify the ordering of the porous patterns in Figs. 10(a) and (c), the coordinates of the pore centers are first captured by the ImagJ software [45] as used before [46], and then the 2D radial distribution function ($RDF = \frac{S_{pattern}}{2\pi r N}\frac{dn(r)}{dr}$) is calculated for each porous pattern, where $S_{pattern}$ is the pattern area, r is the distance between one pore center to a given pore center, N is the total number of pores on the pattern, and $n(r)$ is the number of pores at a distance $\leq r$ from the given pore. In Fig. 10(d), the horizontal axis is normalized by the interpore distance D_{int} of each pattern. From Fig. 10(d), a large difference in the ordering is observed: the top pattern is completely random, with no resemblance of the regular hexagonal structure, while the bottom pattern exhibits short range order up the 7th nearest neighbours. In addition, the interpore distance in the top pattern was found to be about 71 nm, and since the anodization voltage was 40 V, this does not satisfy the 2.5 nm V^{-1} condition compatible for self-ordered growth [2,4]. However, the interpore distance in the bottom pattern was found to be about 105 nm, which satisfies this condition almost exactly. From above analysis, it is clear that although the porous structure is almost disordered at the beginning stage of anodization in Fig.10(a), after 20 hours of self-arrangement process, the porous structure becomes highly ordered as shown in Fig.10(c). This experiment confirms that self-arrangement towards ordering actually happens during anodized growth of anodic porous alumina. The simulation results in

Figs. 8 and 9, in which electric field is considered as the only driving force, successfully predicts this self-ordering growth behavior. Our findings are in agreement with a recent energy-based perturbation analysis [23] in which the electrostatic energy was concluded to be the main driving force for pore initiation as well as a controlling factor for pore spacing selection.

4. Conclusions

Direct numerical simulation of anodic porous alumina growth with two-dimensional pre-textured initial configurations has been performed based on a kinetic model established in the present paper, in which the electric field within the oxide body is considered as the main driving force. Typical features observed in previous experiments, including the linear voltage dependencies of the barrier layer thickness and the pore diameter, the time evolution of the current density under constant voltage, scalloped shape of the oxide barrier layer, and the extreme difference in the reaction rates between pore bottoms and pore walls, have been reproduced in our simulation results. By changing the simulation parameters, three regimes corresponding to nonporous, stable porous and unstable porous oxide growth have been identified. When the simulation parameters are located in stable porous growth regime, pre-textured porous structures which do not satisfy the self-ordering condition are driven by the electric field into self-ordering structures with increasing anodization time. This simulation phenomenon has also been verified by our experiments presented in this paper. The agreement of the present simulation results with experiments suggests that electric field can be the key driving force for porous structure growth as well as self-arrangement towards ordering.

Acknowledgements

Simulations were performed on the HPCPOWER 64-bit (HPCPOWER2) System in the Computer Center of The University of Hong Kong. The authors wish to thank K.Y. Ng and S. Wang for providing the anodization experiments setup. The work described in this paper was supported by grants from the Research Grants Council (Project No. HKU7159/10E), as well as from the University Grants Committee (Project No. SEG-HKU06) of the Hong Kong Special Administration Region, P.R. China.

References

[1] J.P. O’Sullivan, G.C. Wood, Proc. R. Soc. Lond. A 317 (1970) 511.

[2] H. Masuda, K. Fukuda, Science, 268 (1995) 1466.

[3] K. Nielsch, J. Choi, K. Schwim, R.B. Wehrspohn, U. Gosele, Nano Lett. 2 (2002) 677.

[4] W. Lee, R.J.U. Gosele, K. Nielsch, Nature Mater. 5 (2006) 741.

[5] J.E. Houser, K.R. Hebert, Nature Mater. 8 (2009) 415.

[6] H. Masuda, M. Yamada, F. Matsumoto, S. Yokoyama, S. Mashiko, M. Nakao, K. Nishio, Adv. Mater. 18 (2006) 213.

[7] X.Y. Zhang, G.H. Wen, Y.F. Chan, R.K. Zheng, X.X. Zhang, N. Wang, Appl. Phys.

Lett. 83 (2003) 3341.

[8] S.L. Sung, S.H. Tsai, S.H. Tseng, F.K. Chiang, X.W. Liu, H.C. Shih, Appl. Phys. Lett. 74 (1999) 197.

[9] W. Lee, H. Han, A. Lotnyk, M.A. Schubert, S. Senz, M. Alexe, D. Hesse, S. Baik, U. Gosele, Nature Nanotechnology 3 (2008) 402.

[10] T.P. Hoar, N.F. Mott, J. Phys. Chem. Solids 9 (1959) 97.

[11] J. Siejka, C. Ortega, J. Electrochem. Soc. 124 (1977) 883.

[12] C. Cherki, J. Siejka, J. Electrochem. Soc. 120 (1973) 784.

[13] G. Patermarakis, J. Electroanal. Chem. 635 (2009) 39.

[14] V.P. Parkhutik, V.I. Shershulsky, J. Phys. D: Appl. Phys. 25 (1992) 1258.

[15] S.K. Thamida, H.C. Chang, Chaos 12 (2002) 240.

[16] G.K. Singh, A.A. Golovin, I.S. Aranson, V.M. Vinokur, Europhys. Lett. 70 (2005) 836.

[17] G.K. Singh, A.A. Golovin, I.S. Aranson, Phys. Rev. B 73 (2006) 205422.

[18] A.L. Friedman, D. Brittain, L. Menon, J. Chem. Phys. 127 (2007) 154717.

[19] A.L. Friedman, L. Menon, J. Appl. Phys. 101 (2007) 084310.

[20] S.J. Garcia-Vergara, P. Skeldon, G.E. Thompson, H. Habazaki, Electrochim. Acta, 52 (2006) 681.

[21] P. Skeldon, G.E. Thompson, S.J. Garcia-Vergara, L. Iglesias-Rubianes, G. E. Blanco-Pinzon, Electrochem. Solid State Lett. 9(11) (2006) B47.

[22] J. Oh, Ph. D. thesis, Massachusetts Institute of Technology, 2010.

[23] Q.V. Overmeere, F. Blaffart, J. Proost, Electrochem. Commun. 12 (2010) 1174.

[24] J.E. Houser, K.R. Hebert, J. Electrochem. Soc. 153 (2006) B566.

[25] N.Q. Zhao, X.X. Jiang, C.S. Shi, J.J. Li, Z.G. Zhao, X.W. Du, J. Mater. Sci. 42 (2007) 3878

[26] S. Ono, M. Saito, M. Ishiguro, H. Asoh, J. Electrochem. Soc. 151(8) (2004) B473.

[27] J.W. Diggle, T.C. Downie, C.W. Goulding, Chem. Rev. 69 (1969) 365.

[28] M.M. Lohrengel, Mater. Sci. Eng. R 11 (1993) 243.

[29] Z. Wu, C. Richter L. Menon, J. Electrochem. Soc. 154(1) (2007) E8.

[30] N. Cabrera, N.F. Mott, Rep. Prog. Phys. 12 (1949)163.

[31] G. Patermarakis, J. Chandrinos, K. Masavetas, J. Solid State Electrochem, 11 (2007) 1191.

[32] T. Valand, K.E. Heusler, J. Electroanal. Chem. 149 (1983) 71.

[33] G. Patermarakis, K. Moussoutzanis, Electrochim. Acta 54 (2009) 2434.

[34] Matlab R2009a, The Mathworks Inc, Version 7.8.0.347.

[35] Z. Su, W. Zhou, Adv. Mater. 20 (2008) 3663.

[36] M. Nagayama, K. Tamura, Electrochim. Acta 12 (1967) 1097.

[36] W. Lee, J. C. Kim, U. Gosele, Adv. Funct. Mater. 20 (2010) 21.

[37] D. Lo, R. A. Budiman, J. Electrochem. Soc. 154(1) (2007) C60.

[38] F. Li, L. Zhang, R.M. Metzger, Chem. Mater. 10 (1998) 2470.

[40] H. Asoh, K. Nishio, M. Nakao, T. Tamamura, H. Masuda, J. Electrochem. Soc. 148 (2001) B152.

[41] T.P. Hoar, J. Yahalom, J. Electrochem. Soc. 110 (1963) 614.

[42] J.M. Montero-Moreno, M. Sarret, C. Muller, J. Electrochem. Soc. 154(3) (2007) C169.

[43] L. Zaraska, G. D. Sulka, J. Szeremeta, M. Jaskula, Electrochim. Acta 55 (2010) 4377.

[44] K.Y. Ng, Ph. D. thesis, The University of Hong Kong, 2009.

[45] W. Rasband, ImageJ, release 1.36b, NIH: USA, 2006, public domain, http : // rsb.info.nih.gov/ij/.

[46] R. Hillebrand, F. Muller, K. Schwirn, W. Lee, M. Steinhart, ACS Nano 2 (2008) 913.

Figure Captions

Fig. 1. Summary of the reactions assumed at both metal/oxide and oxide/electrolyte interfaces, and the corresponding ion current densities

Fig. 2. Dependence of relative mobile ion density on electric field intensity used in the present simulations, according to Ref. [28].

Fig. 3. Porous structure growth process. (a) t = 0; (b) t = 30 s; (c) t = 75 s; (d) t = 300 s; (e) current density against time corresponding to the growth process. (40 V; B_O = 0.072 A m^{-2}; B_{Al} = 0.72 A m^{-2}, k_O/k_{Al} = 1.5; k_O = 3.8 nm V^{-1}; β = 3/7)

Fig. 4. (a) Current density against time under anodization voltage of 30 V and 50 V, respectively; (b) steady state current density (pore bottom growth rate) against anodization voltage. (B_O = 0.072 A m^{-2}; B_{Al} = 0.72 A m^{-2}, k_O/k_{Al} = 1.5; k_O = 3.8 nm V^{-1}; β = 3/7)

Fig. 5. Barrier layer thickness (pore diameter) against anodization voltage. Dash (dash dotted) line represents the linear fit of barrier layer thickness (pore diameter) against anodization voltage. (B_O = 0.072 A m^{-2}; B_{Al} = 0.72 A m^{-2}, k_O/k_{Al} = 1.5; k_O = 3.8 nm V^{-1}; β = 3/7)

Fig. 6. Porous structures after 300 s anodization time starting from the same

pre-texture in Figure 3(a) under the conditions of (a) B_{Al} = 0.12 A m^{-2}; (b) B_{Al} = 0.36 A m^{-2}; (c) B_{Al} = 0.54 A m^{-2}; (d) B_{Al} = 0.78 A m^{-2}. (e) Current density against time relations corresponding to Figs. 6(a-d), respectively. (40 V; B_O = 0.048 A m^{-2}; $k_O/k_{\rm Al}$ = 1.5; k_O = 3.8 nm V^{-1}; $\beta = 3/7$)

Fig. 7. (a) Map of B_{Al} and B_O conditions for nonporous, stable porous and unstable porous growth to occur; (b) barrier layer thickness against B_{Al} (B_{Al}/B_O ratio in the inset figure); (c) pore diameter against B_{Al}; (d) current density (pore bottom growth rate in the inset figure) against B_{Al}. In (a-d), solid square, solid circle, solid triangle, hollow triangle, and hollow diamond symbols represent B_O equal to 0.024, 0.048, 0.072, 0.096, and 0.120 A m^{-2}, respectively. (40 V; $k_O/k_{\rm Al}$ = 1.5; k_O = 3.8 nm V^{-1}; $\beta = 3/7$)

Fig. 8. Porous structures after 700 s anodization time. The pre-texture contains (a) 1 initial pore; (b) 2 initial pores; (c) 3 initial pores. Except the number of initial pores, other initial dimensions are the same as in Figure 3(a). (d-f) are current density against time corresponding to (a-c), respectively. (40 V; B_O = 0.072 A m^{-2}; B_{Al} = 0.72 A m^{-2}, $k_O/k_{\rm Al}$ = 1.5; k_O = 3.8 nm V^{-1}; $\beta = 3/7$)

Fig. 9. Porous structure growth process staring from a disordered pre-texture. (a) $t = 0$; (b) t = 50 s; (c) t = 100 s; (d) t = 200 s; (e) standard deviation of interpore distance against anodization time. In the pre-texture of figure (a): the sample width, height, barrier layer thickness and pore wall width at the top surface are 900, 83.3, 41.7 and

50 nm, respectively; from the left side, 9 pore diameters are 66.7, 33.3, 50, 66.7, 33.3, 50, 66.7, 33.3, 50 nm, respectively. (40 V; B_{Al} = 0.696 A m^{-2}; B_O = 0.072 A m^{-2}; k_O/k_{Al} = 1.5; k_O = 3.8 nm V^{-1}; β = 3/7)

Fig. 10. SEM micrographs of (a) the top view and (b) the side view of anodic porous alumina. (c) SEM micrograph of the aluminum substrate after removing the anodic porous alumina on top, revealing the pits in the scallop shaped m/o interface. (d) Radial distribution functions for pore distributions in (a), (c) and a reference regular hexagonal structure. Anodization was conducted in 0.4M oxalic acid at 2 ^{o}C at 40V for 20 h.

Figure1

Click here to download high resolution image

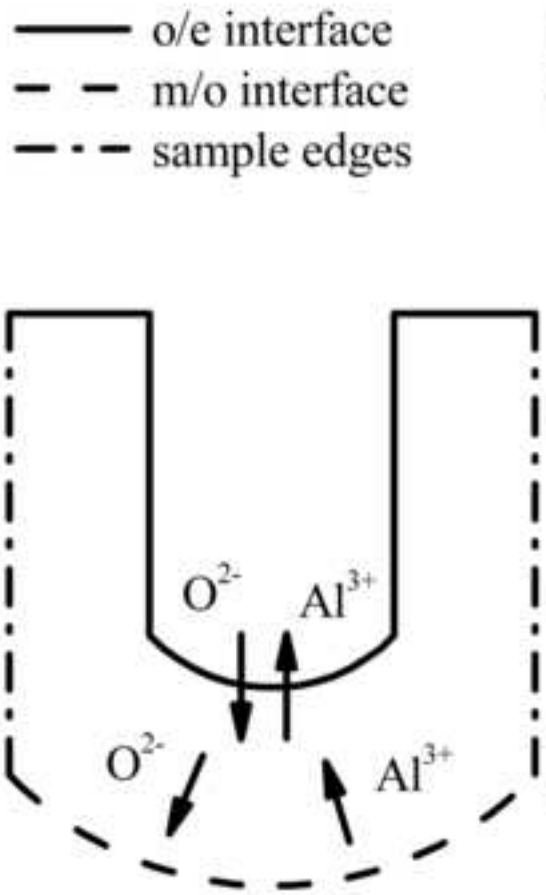

Reactions at o/e interface:	**(Curent density)**
(R2) $Al^{3+}_{(ox)} \rightarrow Al^{3+}_{(aq)}$	Supplied by $\mathbf{j}_{Al,ox}|_{m/o}$ at m/o interface and becomes $\mathbf{j}_{Al,ox}|_{o/e}$ at o/e interface , together with $\mathbf{j}_{Al,dis}$ from oxide decomposition at o/e interface; total value for Al^{3+} across o/e interface is $\mathbf{j}_{Al,o/e} = \mathbf{j}_{Al,ox}|_{o/e} + \mathbf{j}_{Al,dis}$.
(R3) $Al_2O_{3\,(ox)} \rightarrow 2Al^{3+}_{(aq)} + 3O^{2-}_{(ox)}$	Producing $\mathbf{j}_{Al,dis} = \mathbf{j}_{O,dis}$, in which Al^{3+} ejected into electrolyte; O^{2-} migrating towards m/o interface.
(R5) $H_2O_{(aq)} \rightarrow 2H^{+}_{(aq)} + O^{2-}_{(ox)}$	Producing $\mathbf{j}_{O,o/e}$ at o/e interface, in which O^{2-} migrating towards m/o interface.
Reactions at m/o interface:	
(R1) $Al_{(m)} \rightarrow Al^{3+}_{(ox)} + 3e^{-}$	Producing $\mathbf{j}_{Al,ox}|_{m/o}$ at m/o interface, and becomes $\mathbf{j}_{Al,ox}|_{o/e}$ at o/e interface.
(R4) $2Al_{(m)} + 3O^{2-}_{(ox)} \rightarrow Al_2O_{3\,(ox)} + 6e^{-}$	Supplied by $\mathbf{j}_{O,ox}|_{o/e} = \mathbf{j}_{O,o/e} + \mathbf{j}_{O,dis}$ at o/e interface and becomes $\mathbf{j}_{O,ox}|_{m/o}$ at m/o interface.

Ion current density across o/e interface:

Al^{3+} ions ejected into electrolyte: $\mathbf{j}_{Al,o/e} = \mathbf{j}_{Al,ox}|_{o/e} + \mathbf{j}_{Al,dis}$ due to R1, R2 and R3.

O^{2-} ions supplied by electrolyte : $\mathbf{j}_{O,o/e} = \mathbf{j}_{O,ox}|_{o/e} - \mathbf{j}_{O,dis}$ due to R3, R4 and R5.

Figure2

Click here to download high resolution image

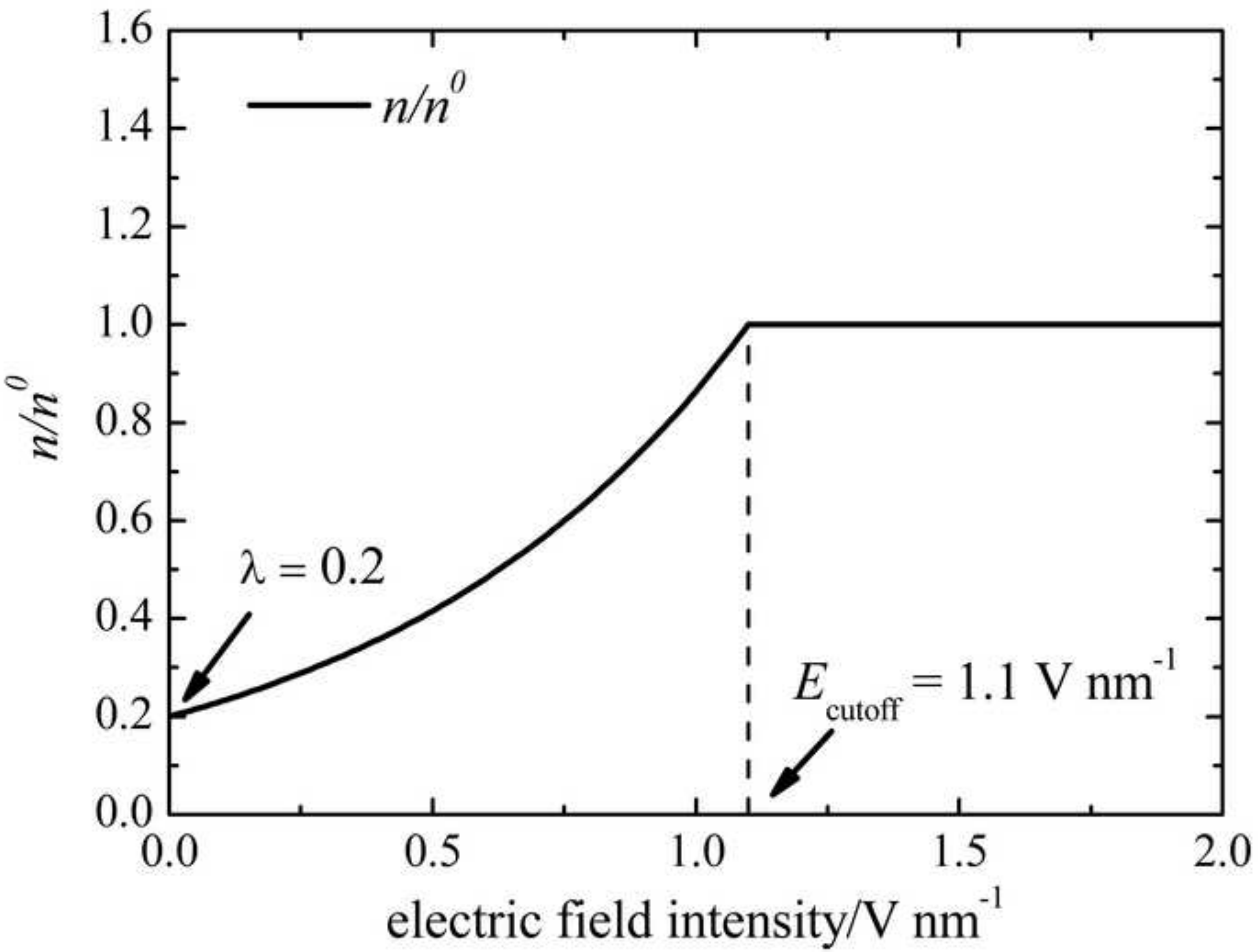

Figure3abcd

Click here to download high resolution image

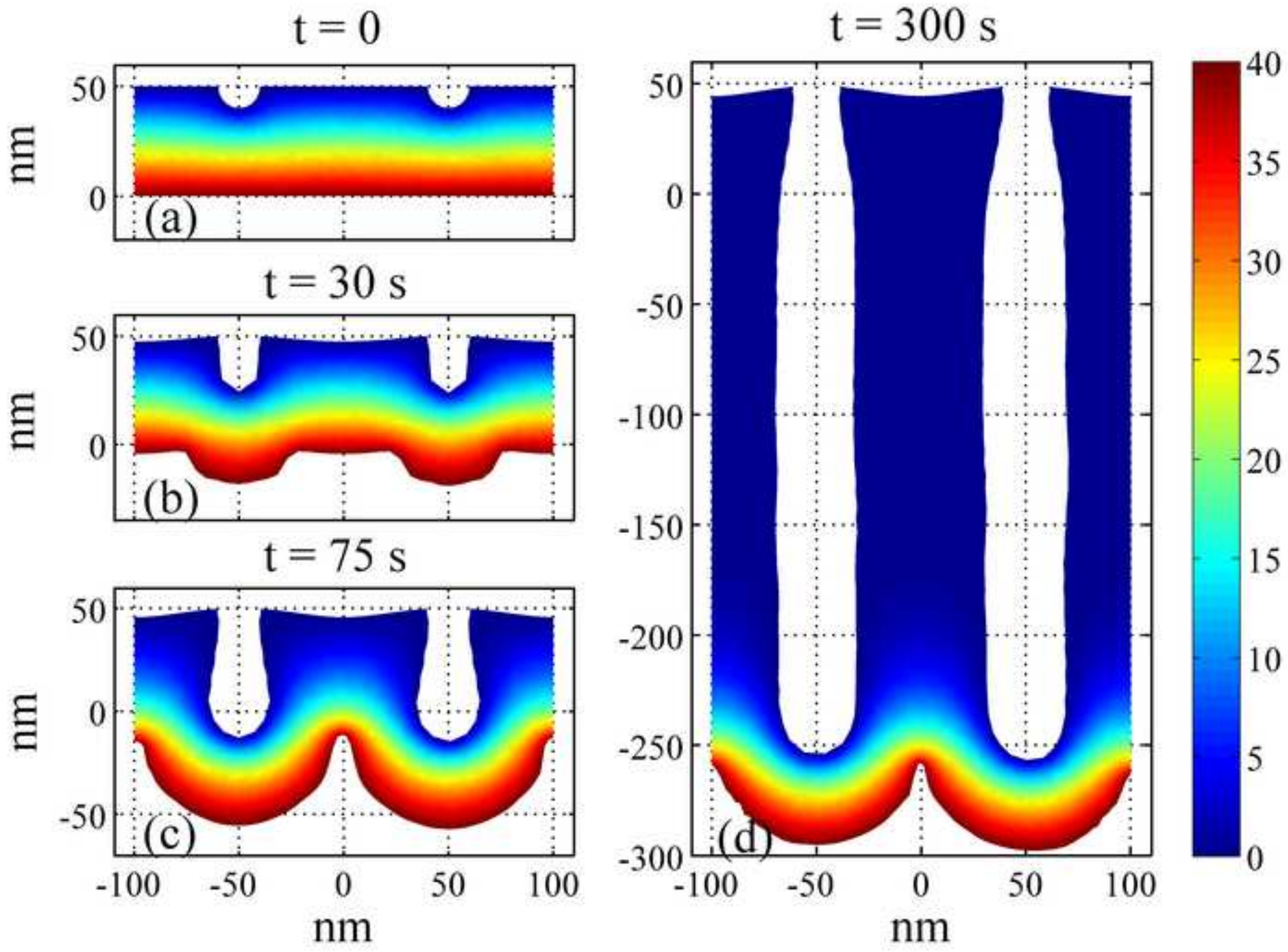

Figure3e

Click here to download high resolution image

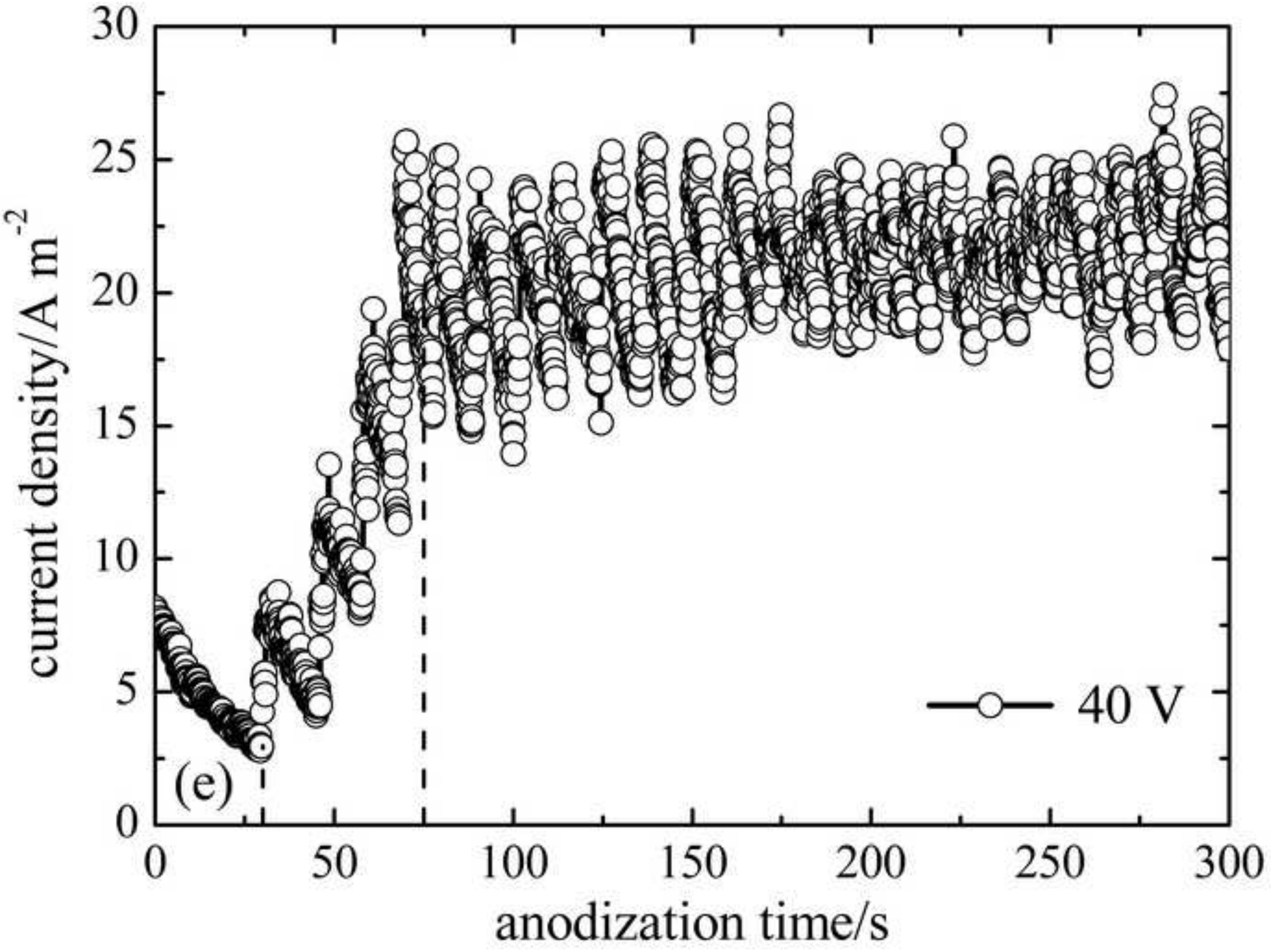

Figure4

Click here to download high resolution image

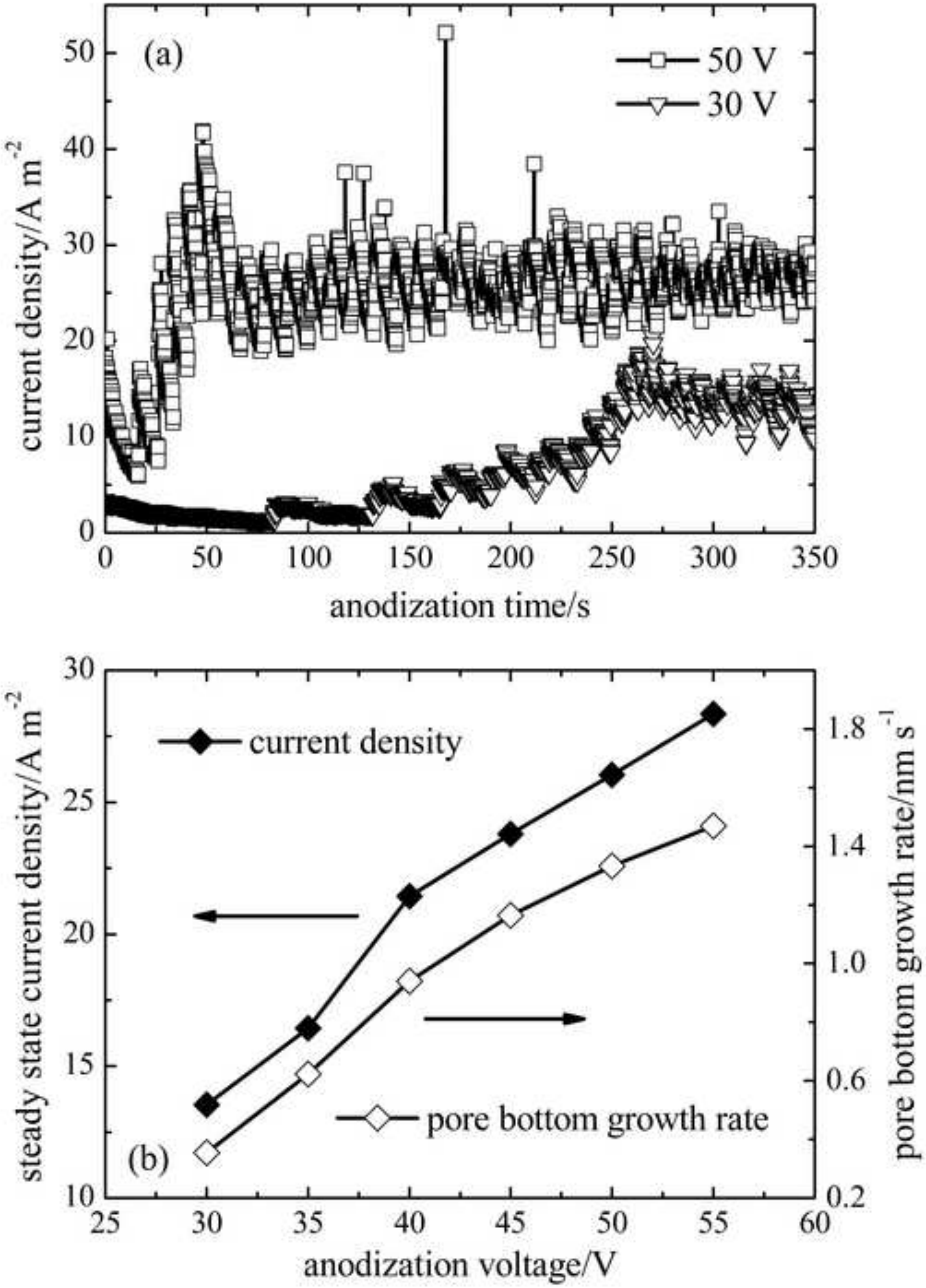

Figure5

Click here to download high resolution image

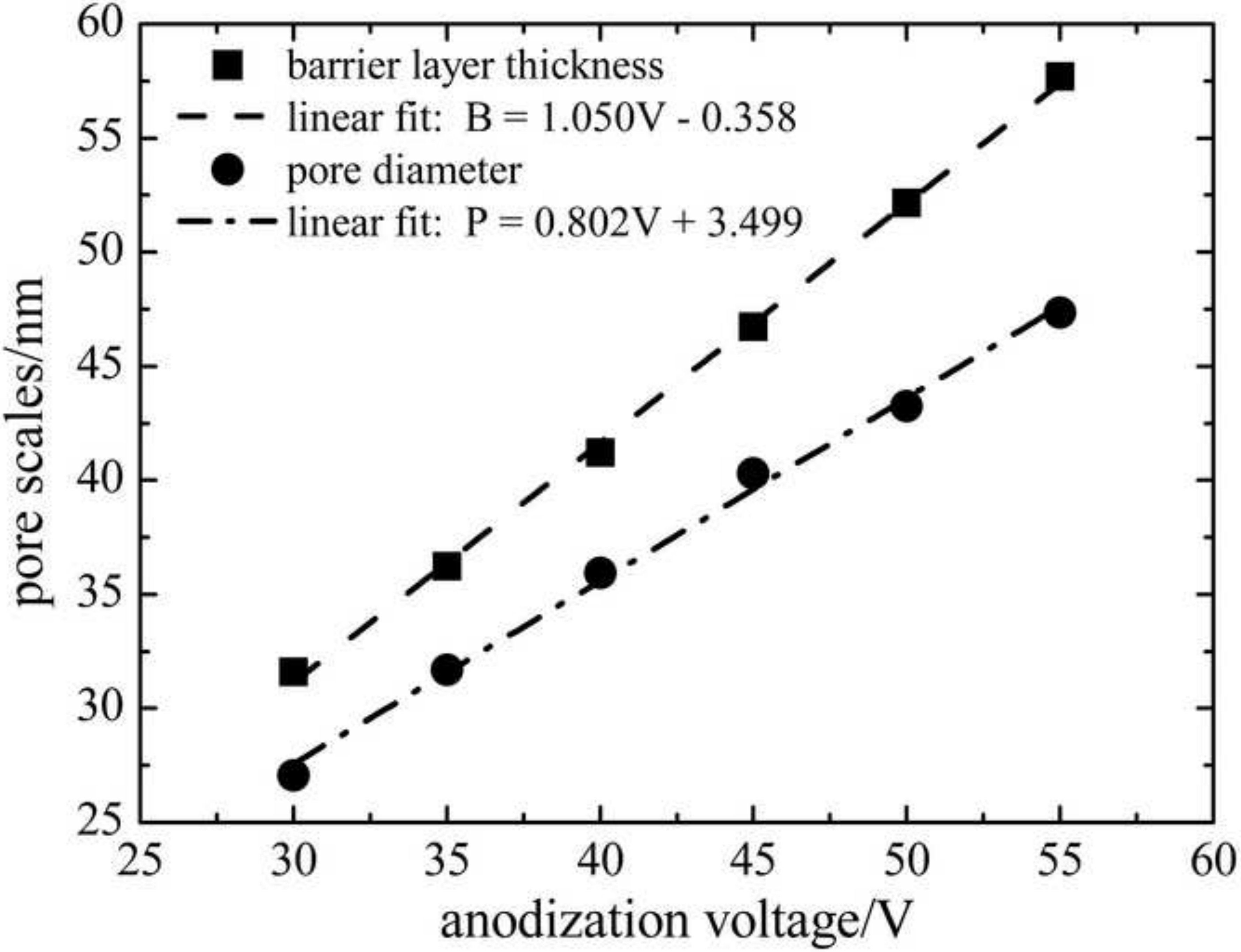

Figure6abcd

Click here to download high resolution image

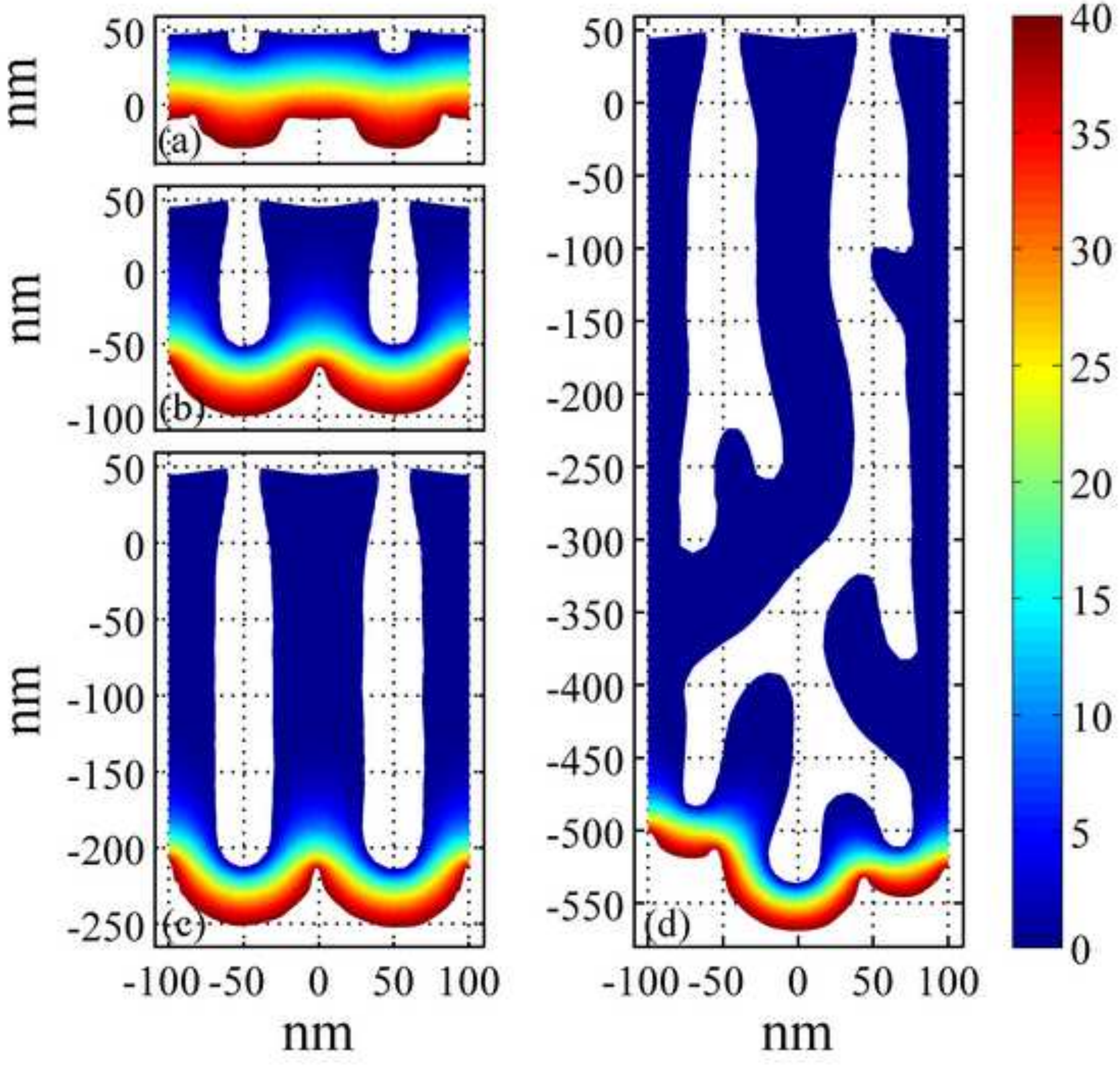

Figure6e

Click here to download high resolution image

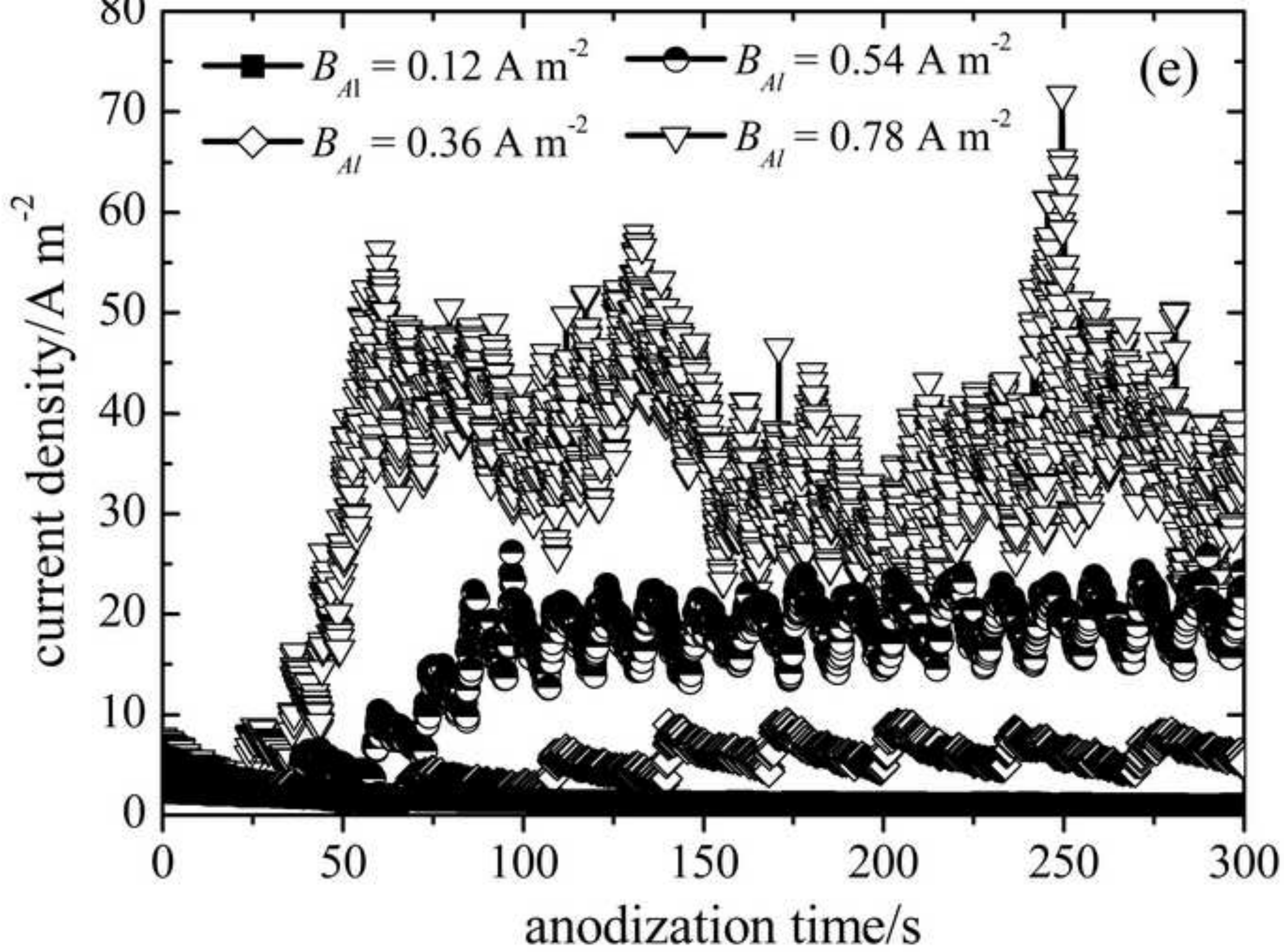

Figure7

Click here to download high resolution image

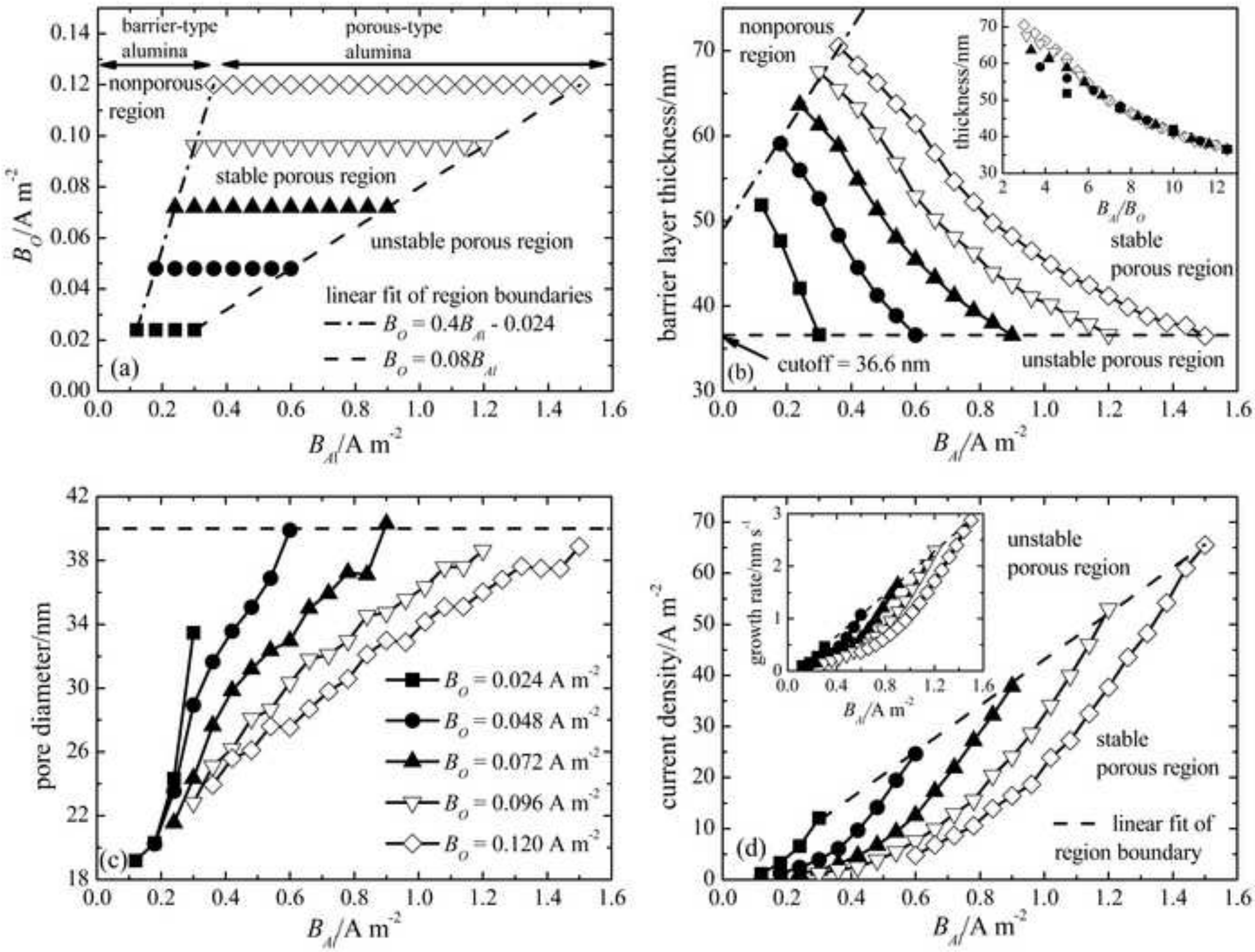

Figure8abc
Click here to download high resolution image

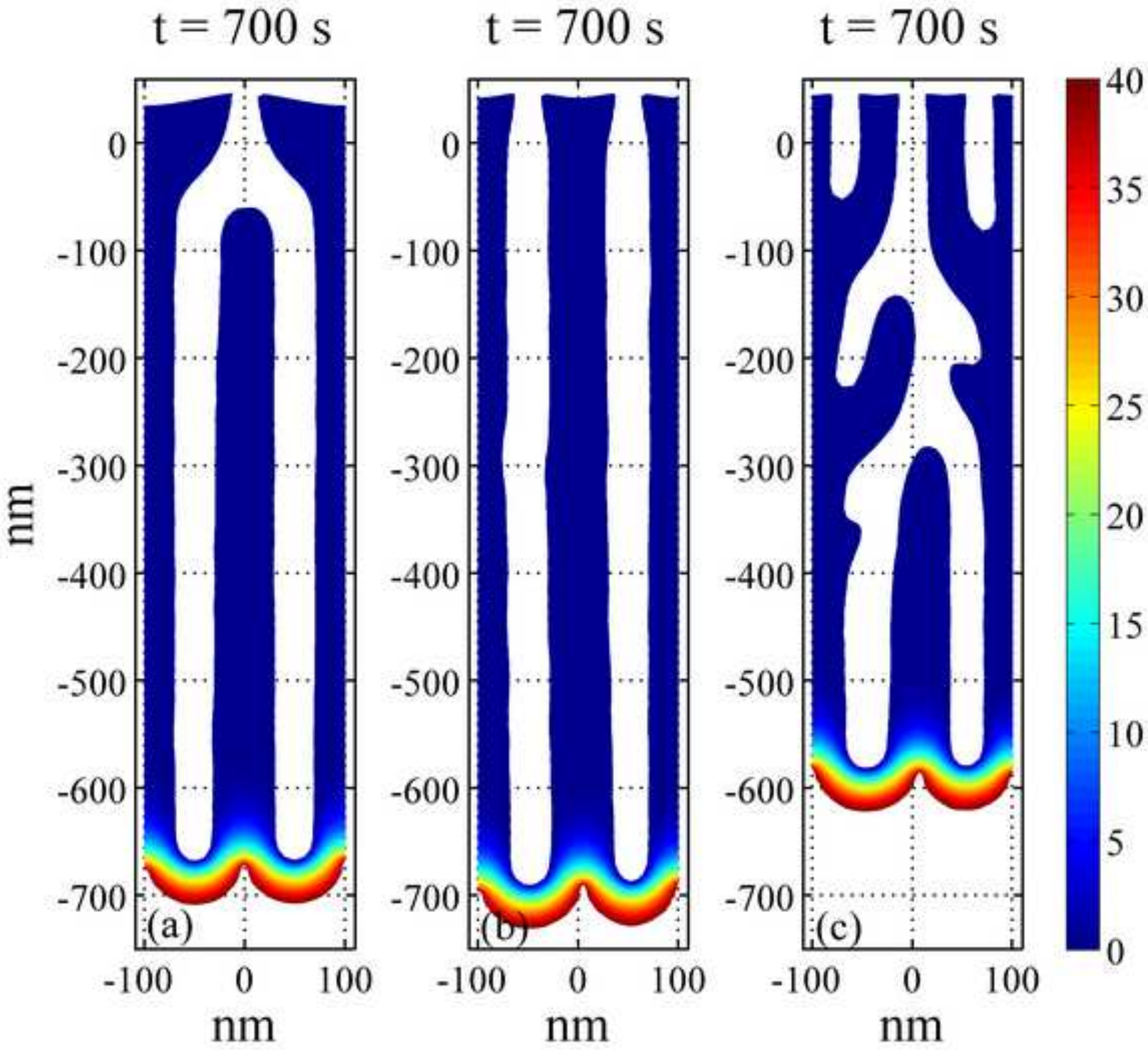

Figure8def

Click here to download high resolution image

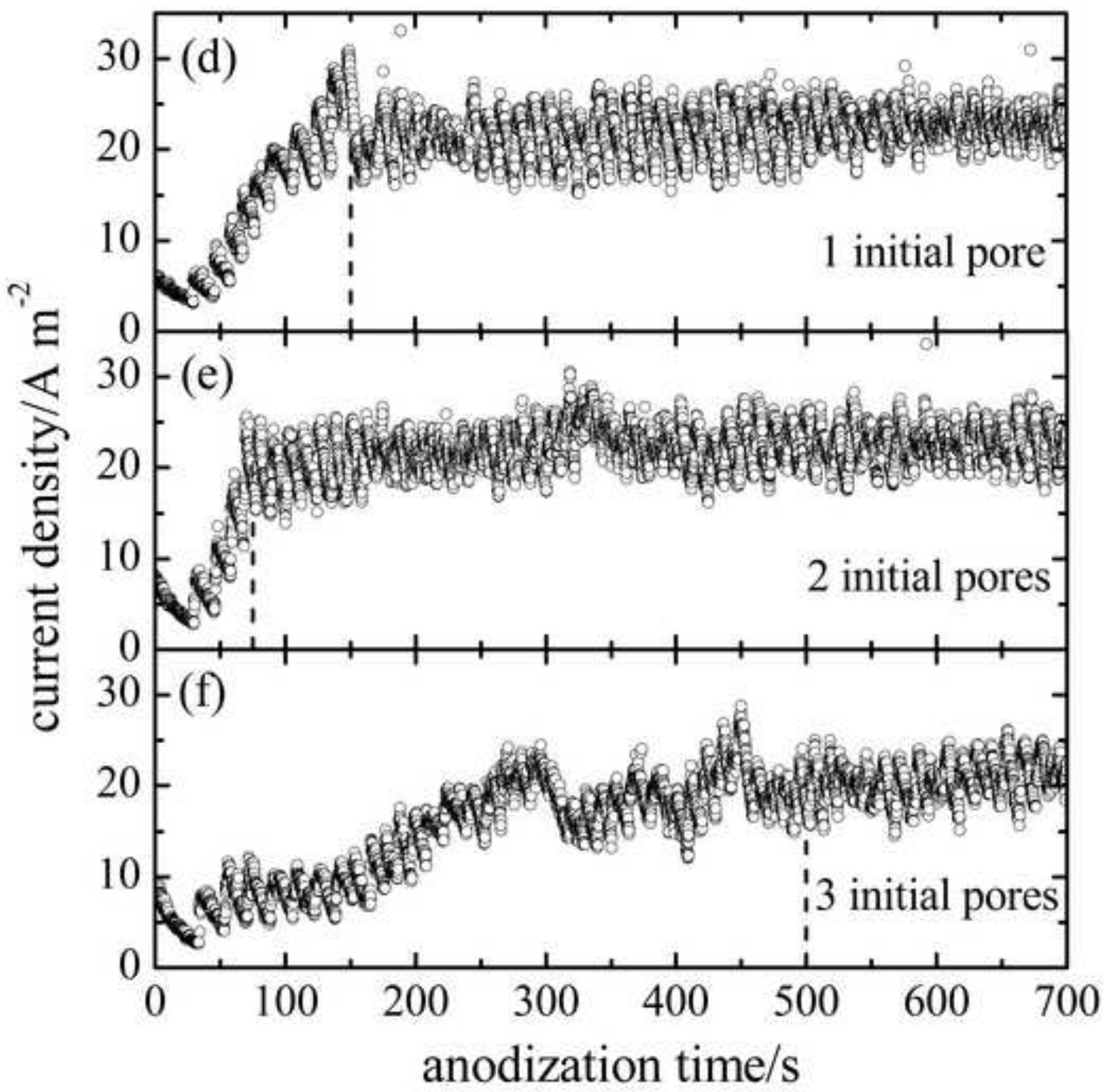

Figure9abcd

Click here to download high resolution image

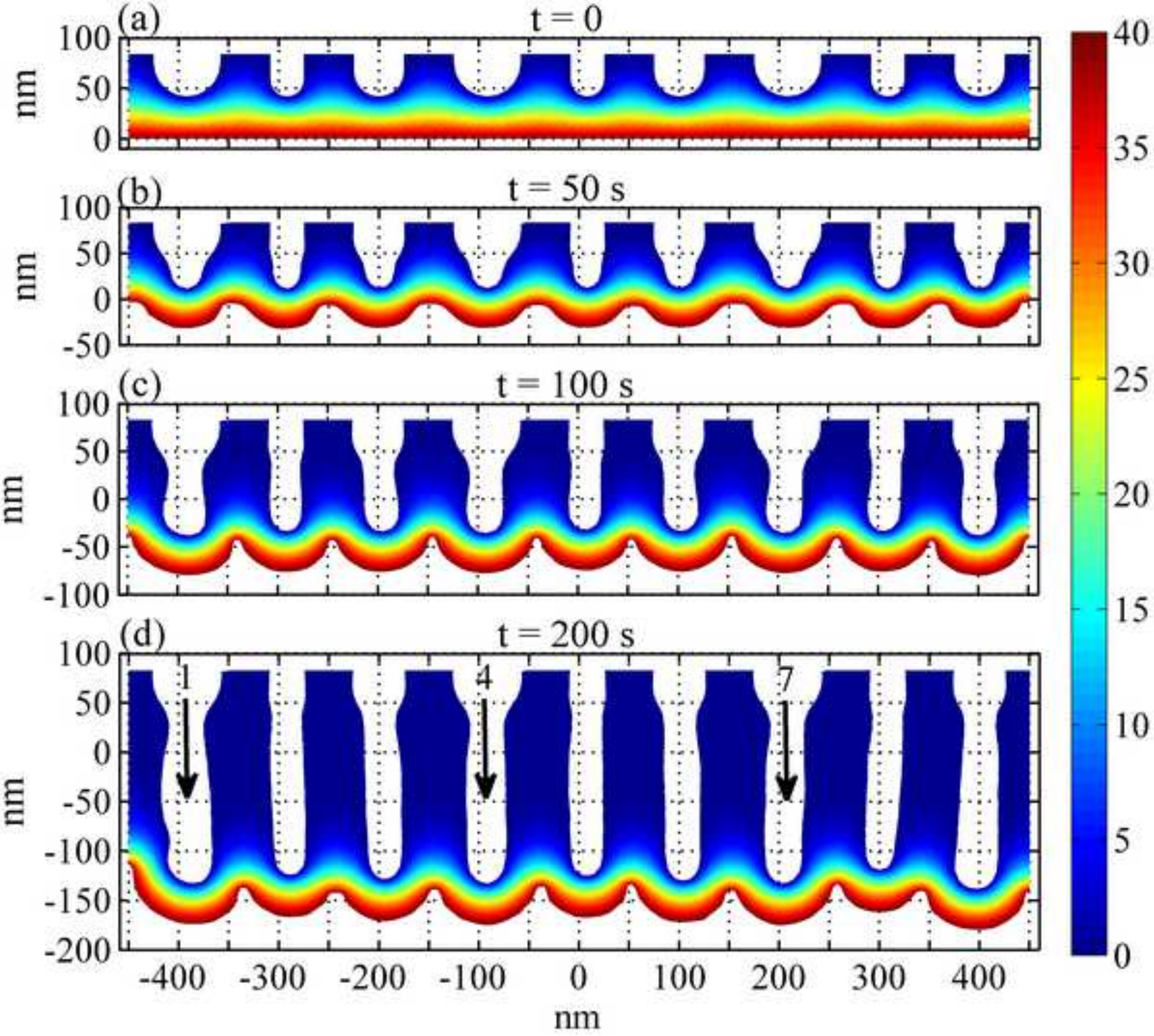

Figure9e

Click here to download high resolution image

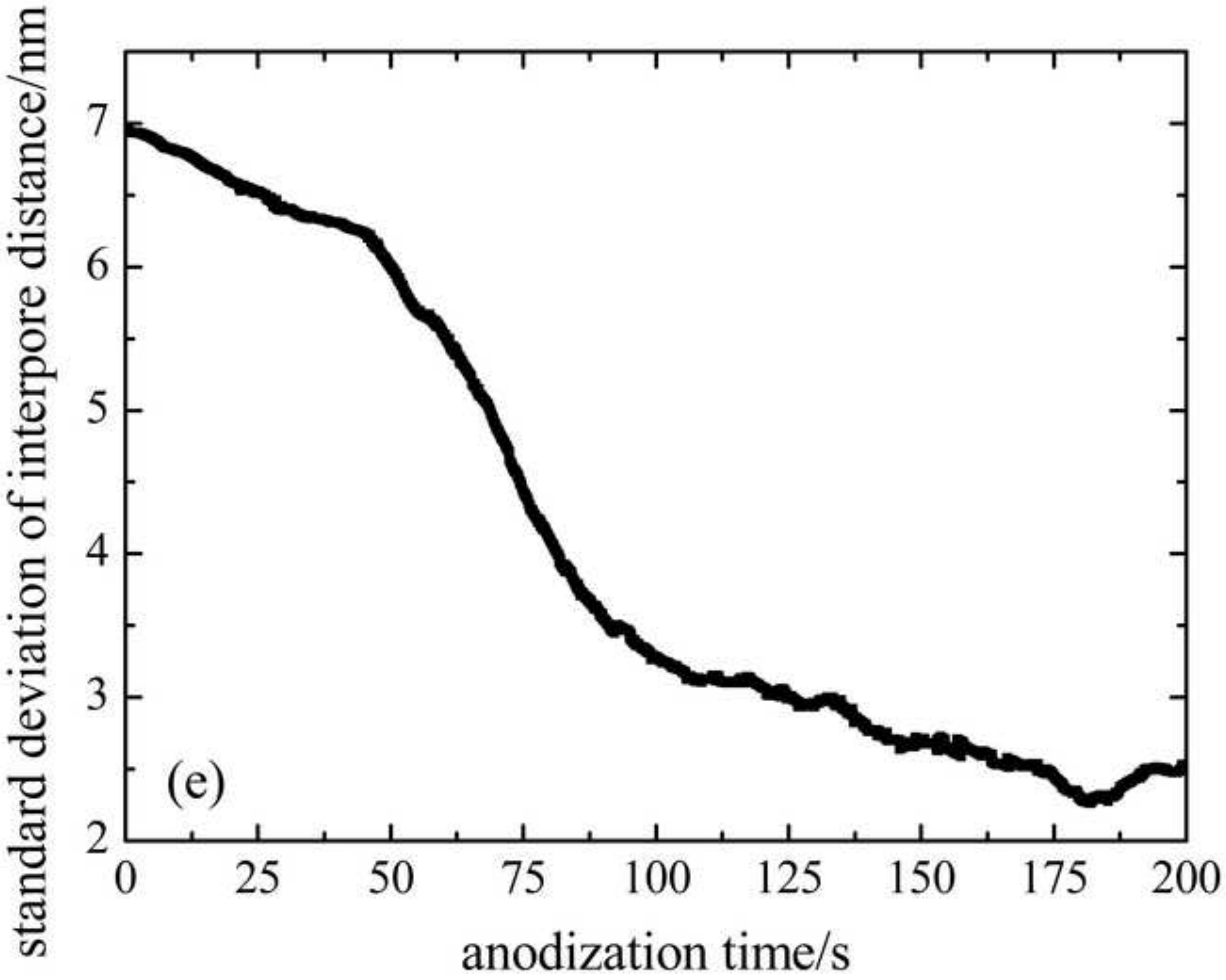

Figure10a

Click here to download high resolution image

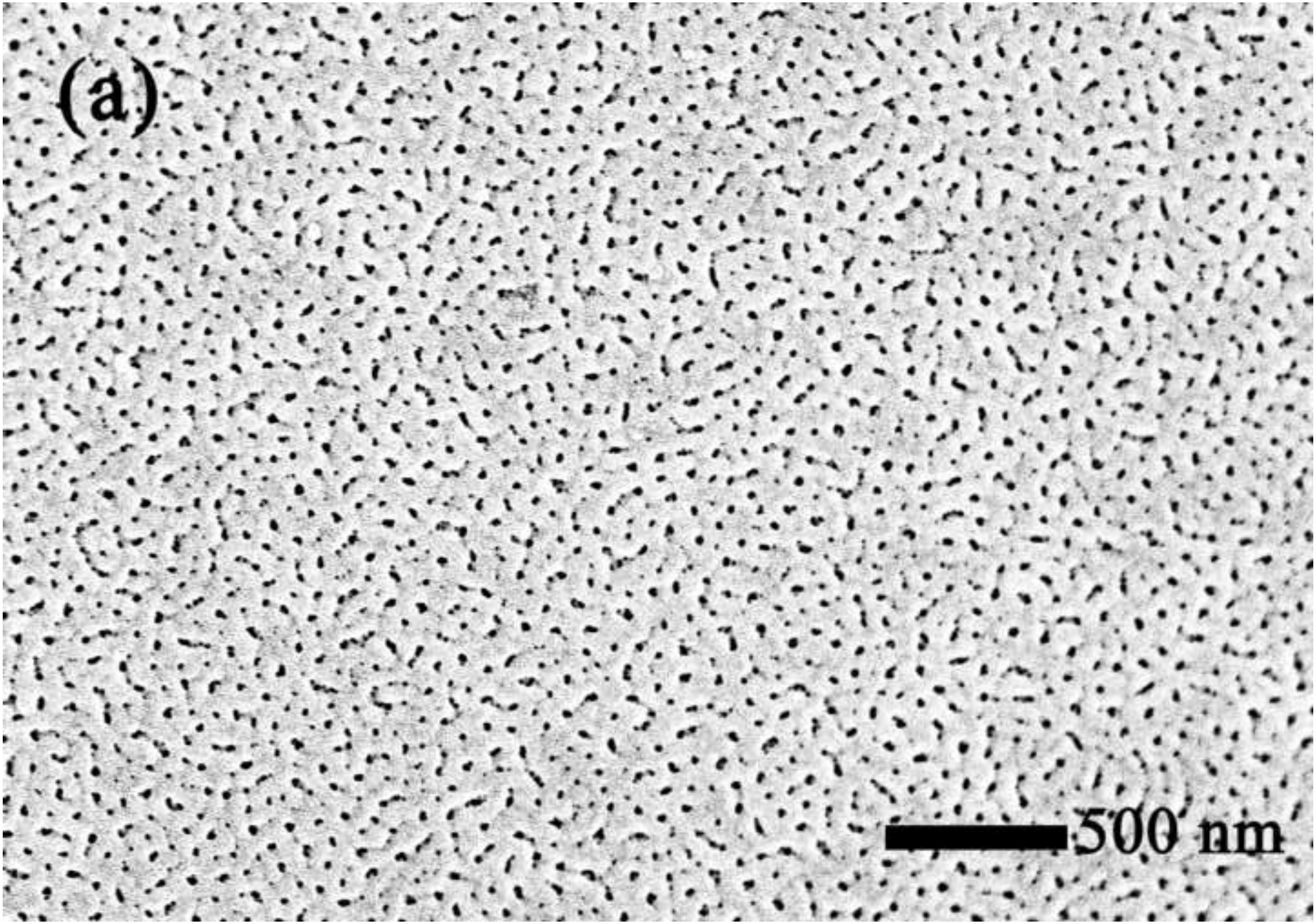

Figure10b

Click here to download high resolution image

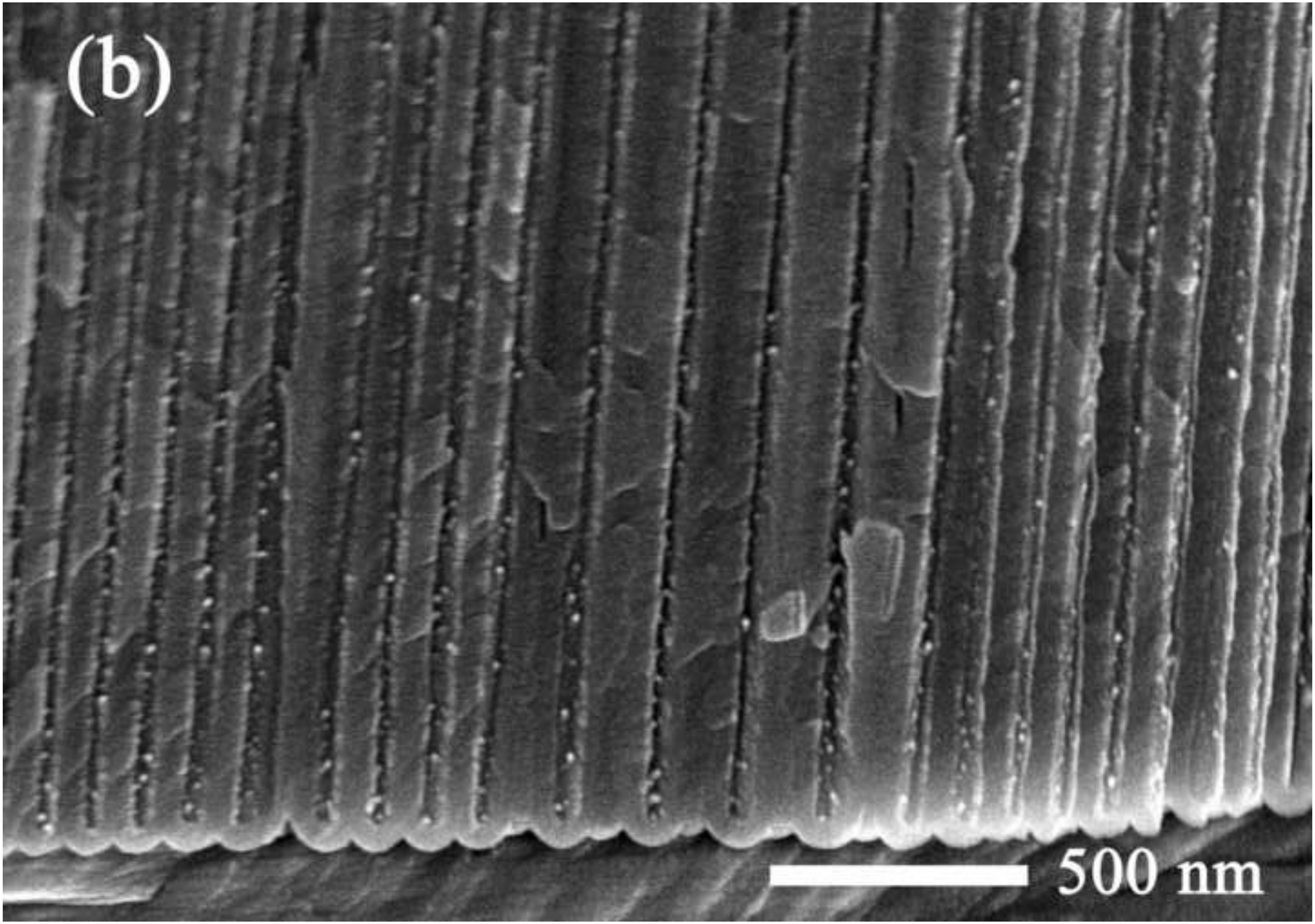

Figure10c

Click here to download high resolution image

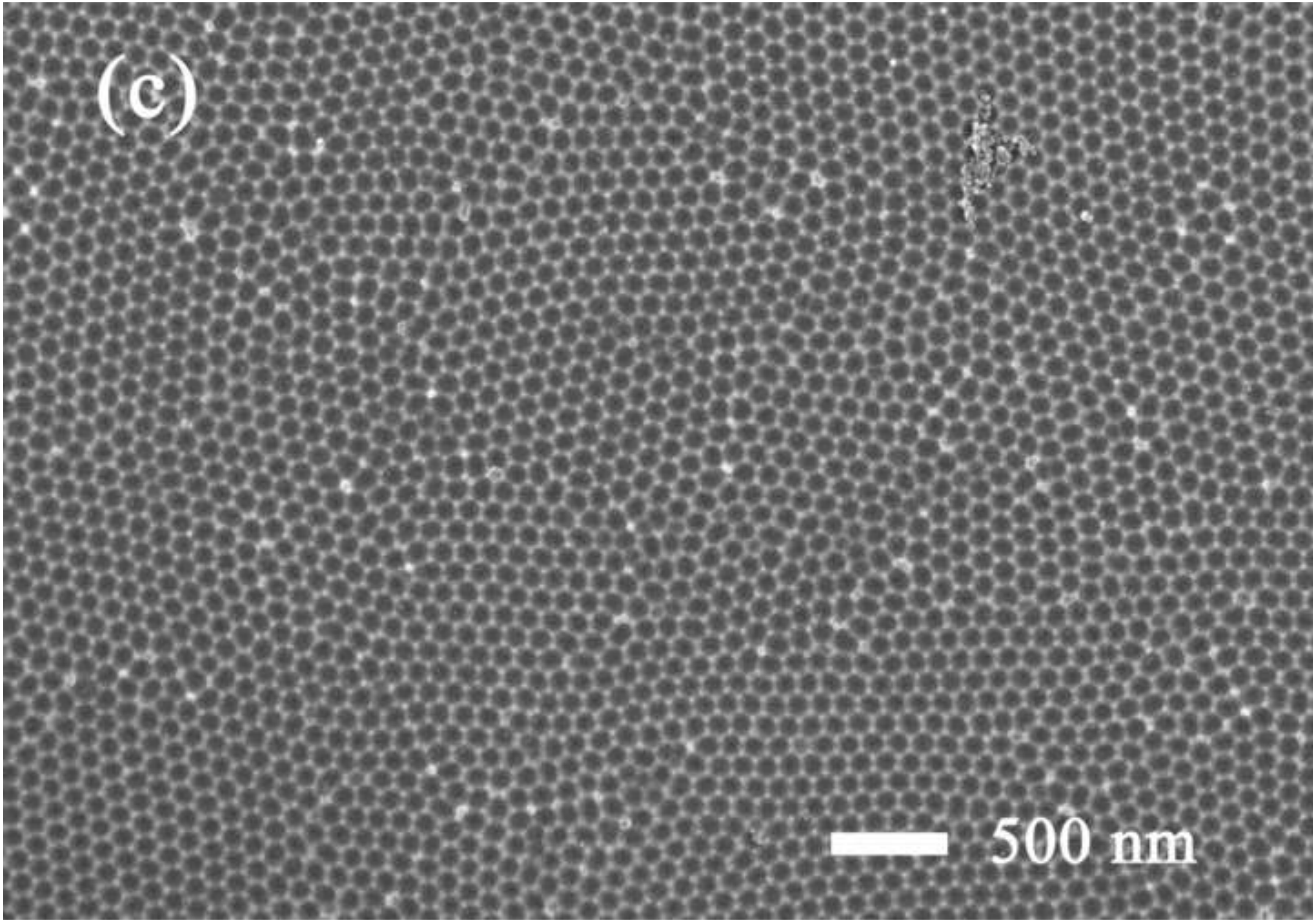

Figure10d

Click here to download high resolution image

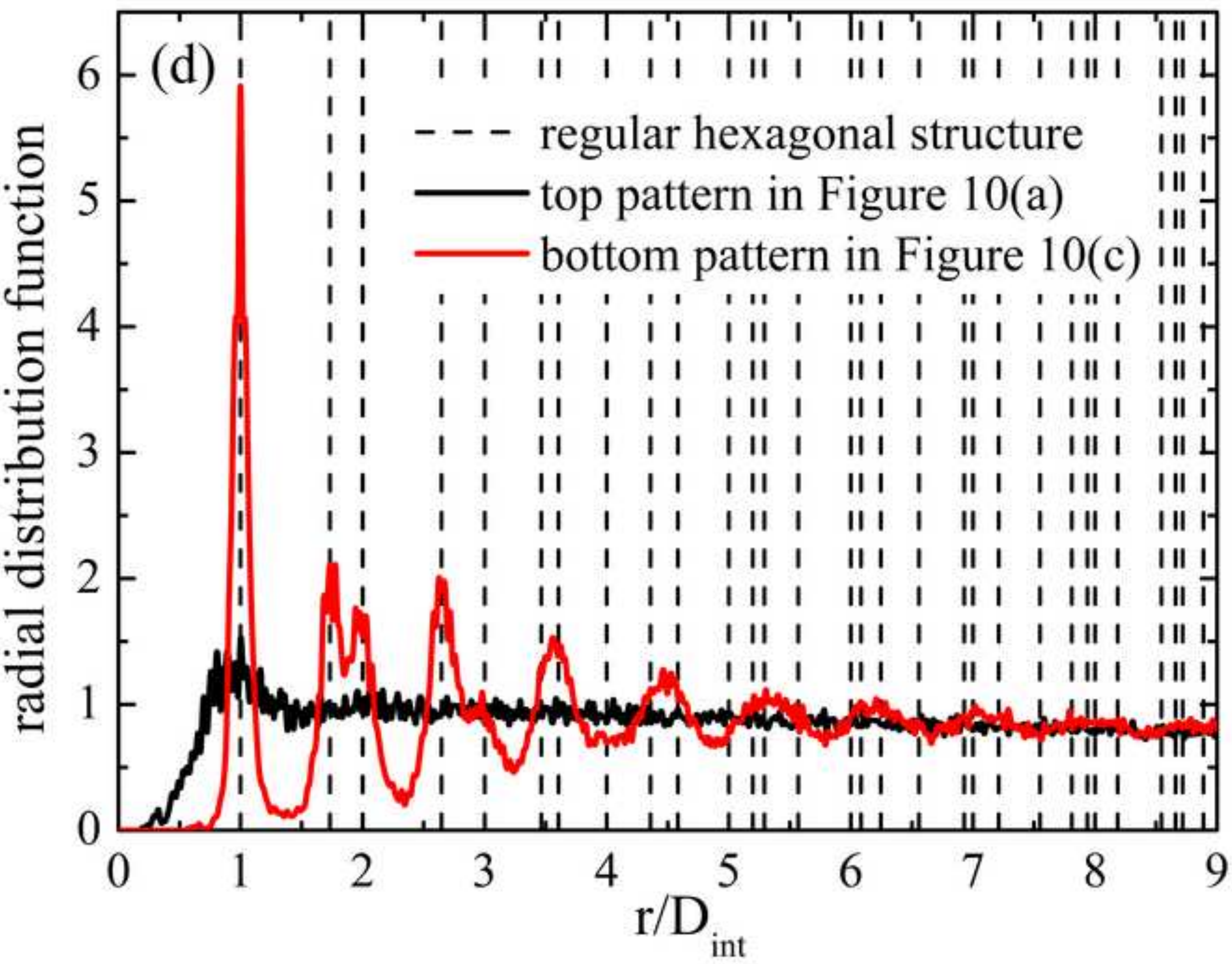

Research Highlights

> We established a kinetic model for anodic porous alumina formation.
> Simulation of real-time porous alumina growth was realized.
> Simulation results agree with typical experimental results very well.
> Nonporous, stable porous and unstable porous regimes of oxide growth are found and the electric field is the main driving force for porous alumina growth and self-ordering.

Previous manuscript NB11-098

Click here to download Supplementary Materials: Previous manuscript NB11-098.pdf